Accepted Manuscript

Assessment of High-Order Finite Volume Methods on Unstructured
Meshes for RANS Solutions of Aeronautical Configurations.

Antonis F. Antoniadis, Panagiotis Tsoutsanis, Dimitris Drikakis

Please cite this article as: Antonis F. Antoniadis, Panagiotis Tsoutsanis, Dimitris Drikakis, Assessment of High-Order Finite Volume Methods on Unstructured Meshes for RANS Solutions of Aeronautical Configurations., *Computers and Fluids* (2017), doi: 10.1016/j.compfluid.2017.01.002

Highlights

- Increased accuracy with WENO high-order discretisation for RANS simulations.

- Improved convergence properties with coupled discretisation of turbulence model.

- WENO 3$^{\text{rd}}$ scheme provides best balance between accuracy, robustness and cost.

- Low-mach number algorithm demonstrates improved solutions for low speed flows.

Assessment of High-Order Finite Volume Methods on Unstructured Meshes for RANS Solutions of Aeronautical Configurations.

Antonis F. Antoniadis[a,*], Panagiotis Tsoutsanis[a], Dimitris Drikakis[b]

[a]*Centre for Computational Engineering Sciences, Cranfield University, Cranfield MK43 0AL, United Kingdom*
[b]*University of Strathclyde, Glasgow, G1 1XW, United Kingdom*

Abstract

This paper is concerned with the application of k-exact finite volume methods for compressible Reynolds-Averaged Navier-Stokes computations of flows around aeronautical configurations including the NACA0012, RAE2822, MDA30P30N, ONERA-M6, CRM and DLR-F11. High-order spatial discretisation is obtained with the Weighted Essentially Non-Oscillatory and the Monotone-Upstream Central Scheme for Conservation Laws methods on hybrid unstructured grids in two- and three- dimensions. Schemes of fifth, third and second order comprise the foundation of the analysis, with main findings suggesting that enhanced accuracy can be obtained with at least a third-order scheme. Steady state solutions are achieved with the implicit approximately factored Lower-Upper Symmetric Gauss-Seidel time advancing technique, convergence properties of each scheme are discussed. The Spalart-Allmaras turbulence model is employed where its discretisation with respect to the high-order framework is assessed. A low-Mach number treatment technique is studied, where recovery of accuracy in low speed regions is exemplified. Results are compared with referenced data and discussed in terms of accuracy, grid dependence and computational budget.

1. Introduction

Reynolds-Averaged Navier-Stokes (RANS) methods are likely to remain the high-fidelity Computational Fluid Dynamics (CFD) modelling approach for the foreseeable future, with second-order discretisation schemes being the most common numerical methods in industrial CFD codes. Advanced turbulence simulations such as Direct Numerical Simulation (DNS) and Large Eddy Simulation (LES) are prohibited in terms of computational cost for high Reynolds number flows around or inside complex geometries.

*Corresponding author
Email addresses: a.f.antoniadis@cranfield.ac.uk (Antonis F. Antoniadis), panagiotis.tsoutsanis@cranfield.ac.uk (Panagiotis Tsoutsanis), dimitris.drikakis@strath.ac.uk (Dimitris Drikakis)

Considerable research efforts have been spent into the development, implementation and assessment of high-order finite volume (FV) discretisation schemes for DNS and LES [1, 2]. High-order methods can achieve at least the same level of accuracy with second-order schemes but using coarser grids [3]. However, the enhanced efficiency is predominantly demonstrated for canonical cases and simple geometrical configurations. In the context of the present study concerning unstructured meshes around simple and complex aeronautical configurations, high-order schemes are referred to spatial discretisation of at least third-order accurate.

In the last decade, accuracy and efficiency considerations were the fundamental drivers for the development of high-order numerical schemes. Recent reviews on high-order methods were presented by Huynh et al. [4] and Wang et al. [5] highlighting the challenges and potential benefits of the methods compared with production codes. The vast majority of high-order schemes are based on the finite volume and the discontinuous Galerkin (DG) numerical frameworks. Other methods include the DG spectral element [6, 7] and hybrid DG/FV methods [8–10]. High-order methods combined with solution adaptive techniques such as grid refinement and/or order enrichment demonstrate promising results on unstructured grids [11, 12]. The essentially non-oscillatory (ENO) and weighted-ENO (WENO) schemes were originally formulation for FV methods [13–15] for structured grids [16, 17]. Furthermore, several research groups extended the original schemes to handle unstructured [18–22] as well as mixed-element unstructured grids [3, 23–26], furthermore WENO methods are also utilised within the DG framework [27, 28].

WENO schemes have been mainly used for inviscid, laminar and low Reynolds number flows [29, 30]. The grid requirements of high Reynolds number flows combined with low-quality highly skewed geometric elements poses a considerable robustness challenge for any high-order numerical method. For WENO schemes the grid sensitivity is mainly due to the inherited spatial extensiveness of the scheme, requiring large stencils for the reconstruction process. Furthermore, meshes with small neighbouring surface/volume ratio will benefit more as higher-order approximation of derivatives and gradient will be accurately estimated. The scheme is less sensitive to individual geometric quality metrics, as opposed to other framework, such as DG, where high-order grids would be required in order to explore their full potential of the method [31]. High-order spatial representation is a promising field, however for complex configurations often encounter in external aerodynamics, there is a limited number of tools available for accurate and efficient generation of high-order, curved meshes.

Numerical convergence and accuracy of CFD simulations can be further compromised by insufficient grid resolution, numerical dissipation and turbulence modelling issues. Furthermore, low Mach number effects can become important in near wall regions as well as in flow regions where vortical structures are

3

dominant [32, 33]. Numerical methods designed for compressible flows should be assessed for their accuracy in these flow regions. Slow convergence rates and excessive numerical dissipation are often encountered in problems encompassing large changes in wave speeds. Local preconditioning methods [34, 35] are popular techniques to address the stiffness of the resulting non-linear system. However, the computational expense can be excessive particularly for complex flow phenomena [36] such as unsteadiness, shock-wave-boundary layer interaction, transition and turbulence, which are often associated with buffet and flutter effects. A more compact technique with considerable smaller computational overhead was proposed by Thornber et al. [32] for block-structured grids and was investigated for a broad range of flows in [2]. The method was also employed in conjunction with implicit time-stepping in [37].

Implementation of high-order methods in conjunction with turbulence models poses additional challenges with respect to robustness, accuracy and efficiency. High-order discretisation of the turbulence model transport equations can lead to non-physical (negative) eddy viscosity values, numerical artefacts and slow convergence rates [38]. Several researchers have documented irregularities attributed to the boundary layer edge-singularity inherited within wall-distance dependent turbulence models [39].

The development and implementation of the present high-order WENO and MUSCL schemes for unstructured grids has been presented for inviscid applications in [23]; for laminar, transitional and turbulent canonical and simple geometrical flows in the framework of Implicit Large Eddy Simulation (ILES) in [3] using an explicit time stepping technique. Although the utilisation of high-order methods makes more sense for long-time evolution of unsteady turbulent flow simulations, we explore the benefits that they can offer in the context of RANS simulations. Since in theory they should be able to provide smaller errors with respect to grid resolution, hence significant savings in terms of computational time. This paper assesses both the accuracy and efficiency of second- and third-order variants of the MUSCL scheme in conjunction with total variation diminishing (TVD) limiter functions as well as third- and fifth-order WENO schemes on mixed-element unstructured grids for subsonic and transonic flows around single aerofoils; multi-element aerofoils at high angle incidence; 3D wing; and aircraft configurations at cruise and landing conditions. The RANS computations have been carried out using an implicit lower-upper symmetric Gauss-Seidel (LU-SGS) method [40, 41] and the one-equation Spalart-Allmaras (SA) turbulence model [42]. The paper is organized as follows. Section 2 is dedicated to the governing equations, Section 3 presents the high-order finite volume framework for unstructured meshes, the MUSCL and WENO methods, the flux treatment, the implicit time-stepping algorithm and the low-Mach number treatment method. The numerical results obtained for all the test-cases are presented in Sections 4. The conclusions drawn from the present study are outlined in

4

the last section.

2. Governing Equations

The compressible RANS equations with the one-equation Spalart-Allmaras (SA) turbulence model are written in conservative form as:

$$\frac{\partial \mathbf{U}(\mathbf{x},t)}{\partial t} + \nabla(\mathbf{F_c}(\mathbf{U}) - \mathbf{F_v}(\mathbf{U}, \nabla \mathbf{U})) = \mathbf{S}(\mathbf{U}, \nabla \mathbf{U}), \tag{1}$$

where $\mathbf{U}$ is the vector of the conserved mean flow variables and the turbulence model variable, and $\mathbf{F_c}$ and $\mathbf{F_v}$ are the inviscid and viscous flux vectors, respectively:

$$
\begin{aligned}
\mathbf{U} &= \left[\rho, \rho u, \rho v, \rho w, E, \tilde{\nu}\right]^T, \\
\mathbf{F}_c^{\mathbf{x}} &= \left[\rho u, \rho u^2 + p, \rho uv, \rho uw, u(E+p), u\tilde{\nu}\right]^T, \\
\mathbf{F}_c^{\mathbf{y}} &= \left[\rho v, \rho uv, \rho v^2 + p, \rho vw, v(E+p), v\tilde{\nu}\right]^T, \\
\mathbf{F}_c^{\mathbf{z}} &= \left[\rho w, \rho uw, \rho vw, \rho w^2 + p, w(E+p), w\tilde{\nu}\right]^T, \\
\mathbf{F}_v^{\mathbf{x}} &= \left[0, \tau_{xx}, \tau_{xy}, \tau_{xz}, \Theta_x, \frac{1}{\sigma}(\nu_l + \tilde{\nu})\frac{\partial \tilde{\nu}}{\partial x}\right]^T, \\
\mathbf{F}_v^{\mathbf{y}} &= \left[0, \tau_{xy}, \tau_{yy}, \tau_{yz}, \Theta_y, \frac{1}{\sigma}(\nu_l + \tilde{\nu})\frac{\partial \tilde{\nu}}{\partial y}\right]^T, \\
\mathbf{F}_v^{\mathbf{z}} &= \left[0, \tau_{xz}, \tau_{yz}, \tau_{zz}, \Theta_z, \frac{1}{\sigma}(\nu_l + \tilde{\nu})\frac{\partial \tilde{\nu}}{\partial z}\right]^T, \\
\mathbf{S} &= \left[0, 0, 0, 0, 0, C_{b1}\tilde{S}\tilde{\nu} + \frac{1}{\sigma}C_{b2}\left(\nabla \tilde{\nu}\right)^2 - C_{w1}f_w\left(\frac{\tilde{\nu}}{d}\right)^2\right]^T.
\end{aligned}
\tag{2}
$$

In the above equations, ρ is the density, u, v, w are the velocity components in x, y and z Cartesian coordinates, respectively. Calorically perfect gas is assumed where the total energy per unit volume is calculated by $E = p/(\gamma - 1) + (1/2)\rho(u^2 + v^2 + w^2)$, where p is the pressure, $\gamma = 1.4$ is the ratio of specific heats for air at normal atmospheric conditions; ν is the kinematic laminar viscosity and $\tilde{\nu}$ is the SA turbulent viscosity working variable. The laminar viscosity is related to the temperature through the Sutherland law:

$$\frac{\mu_l}{\mu_0} = \left(\frac{T}{T_0}\right)^{\frac{3}{2}} \frac{T_0 + S}{T + S}, \tag{3}$$

S is the Sutherland temperature and the subscript 0 denotes a reference state for the corresponding variables. Unless otherwise stated, the reference values are taken at atmospheric conditions (sea level): dynamic viscosity $\mu_0 = 1.7894 \times 10^{-5} kg/(ms)$; reference temperatures $T_0 = 288.16K$; $S = 110.4K$; and Prandtl

number $Pr = 0.72$. Using the Boussinesq's approximation the viscous stress tensor τ_{ij} is defined by

$$\tau_{ij} = (\mu_l + \mu_t)\left(\frac{\partial \mathbf{u}_i}{\partial \mathbf{x}_j} + \frac{\partial \mathbf{u}_j}{\partial \mathbf{x}_i} - \frac{2}{3}\frac{\partial \mathbf{u}_k}{\partial \mathbf{x}_k}\delta_{ij}\right), \tag{4}$$

where μ_t is the eddy viscosity, δ_{ij} is the Kronecker delta and the subscripts i, j, k refer to the Cartesian coordinate components $\mathbf{x} = (x, y, z)$. The work of viscous stresses and heat conduction, Θ, is given by:

$$\begin{aligned}
\Theta_x &= u\tau_{xx} + v\tau_{xy} + w\tau_{xz} + \left(\frac{\mu}{Pr} + \frac{\mu_t}{Pr_t}\right)\frac{\gamma}{(\gamma-1)}\frac{\partial T}{\partial x}, \\
\Theta_y &= u\tau_{yx} + v\tau_{yy} + w\tau_{yz} + \left(\frac{\mu}{Pr} + \frac{\mu_t}{Pr_t}\right)\frac{\gamma}{(\gamma-1)}\frac{\partial T}{\partial y}, \\
\Theta_z &= u\tau_{zz} + v\tau_{zy} + w\tau_{zz} + \left(\frac{\mu}{Pr} + \frac{\mu_t}{Pr_t}\right)\frac{\gamma}{(\gamma-1)}\frac{\partial T}{\partial z}.
\end{aligned} \tag{5}$$

Pr_t is the turbulent Prandtl number; ν_t is the turbulent kinematic viscosity. The SA turbulence working variable $\tilde{\nu}$ is related to eddy viscosity μ_t by:

$$\mu_t = \rho\tilde{\nu}f_{v1}, \quad \text{where} \quad f_{v1} = \frac{(\rho\tilde{\nu}/\mu_l)^3}{(\rho\tilde{\nu}/\mu_l)^3 + C_{v1}^3} \quad \text{and} \quad C_{v1} = 7.1. \tag{6}$$

where the component of the source term $\mathbf{S}$ of equation (2) are given as:

$$\tilde{S} = \Omega + f_{v2}\frac{\tilde{\nu}}{\kappa^2 d^2}, \quad f_{v2} = 1 - \frac{(\rho\tilde{\nu}/\mu_l)}{1 + (\rho\tilde{\nu}/\mu_l)f_{v1}}, \tag{7}$$

Ω is the vorticity magnitude and

$$f_w = g\left(\frac{1 + C_{w3}^6}{g^6 + C_{w3}^6}\right)^{1/6}, \quad \text{where} \quad g = r + C_{w2}\left(r^6 - r\right) \quad \text{and} \quad r = min\left(\frac{\tilde{\nu}}{\tilde{S}\kappa^2 d^2}, r_{lim}\right). \tag{8}$$

The closure constants are:

$$\begin{aligned}
C_{b2} &= 0.622, \quad C_{w1} = \frac{C_{b1}}{\kappa^2} + \frac{1 + C_{b2}}{\sigma}, \quad C_{w2} = 0.3, \\
C_{b1} &= 0.1355, \quad C_{w3} = 2.0, \quad \sigma = 2/3, \quad \kappa = 0.41, \quad r_{lim} = 10, \quad Pr_t = 0.9.
\end{aligned} \tag{9}$$

as given in [42].

3. Numerical Framework

The discretisation in a domain Ω is achieved by combining conforming arbitrary shaped elements of volume $|V_i|$. Integrating equation (1) over a mesh element using the finite volume formulation the following

6

ordinary differential equation is obtained

$$
\begin{aligned}
\frac{d\mathbf{U}_i}{dt} = & -\frac{1}{|V_i|} \sum_{l=1}^{N_f} \sum_{\alpha=1}^{N_{qp}} \mathbf{F}_c^{\mathbf{n,l}} \left(\mathbf{U}(\mathbf{x}_\alpha, t) \right) \omega_\alpha |A_l| \\
& + \frac{1}{|V_i|} \sum_{l=1}^{N_f} \sum_{\alpha=1}^{N_{qp}} \mathbf{F}_v^{\mathbf{n,l}} \left(\mathbf{U}(\mathbf{x}_\alpha, t), \nabla \mathbf{U}(\mathbf{x}_\alpha, t) \right) \omega_\alpha |A_l| + \mathbf{S}_i,
\end{aligned}
\tag{10}
$$

where $\mathbf{U}_i$ is the volume averaged conserved variable vector, $\mathbf{S}_i$ is the volume averaged source term vector within in a volume element i, N_f is the number of faces per element, N_{qp} is the number of quadrature points used for approximating the surface integrals. Figure 1 illustrates an example of quadrature point distribution on a aircraft surface mesh; the blue points located near the vertices correspond to quadrature weight smaller compared with the points located in the midsection coloured in red. $|A_l|$ is the surface area of the corresponding face, and α corresponds to different Gaussian integration points $\mathbf{x}_\alpha$ and weights ω_α over the face.
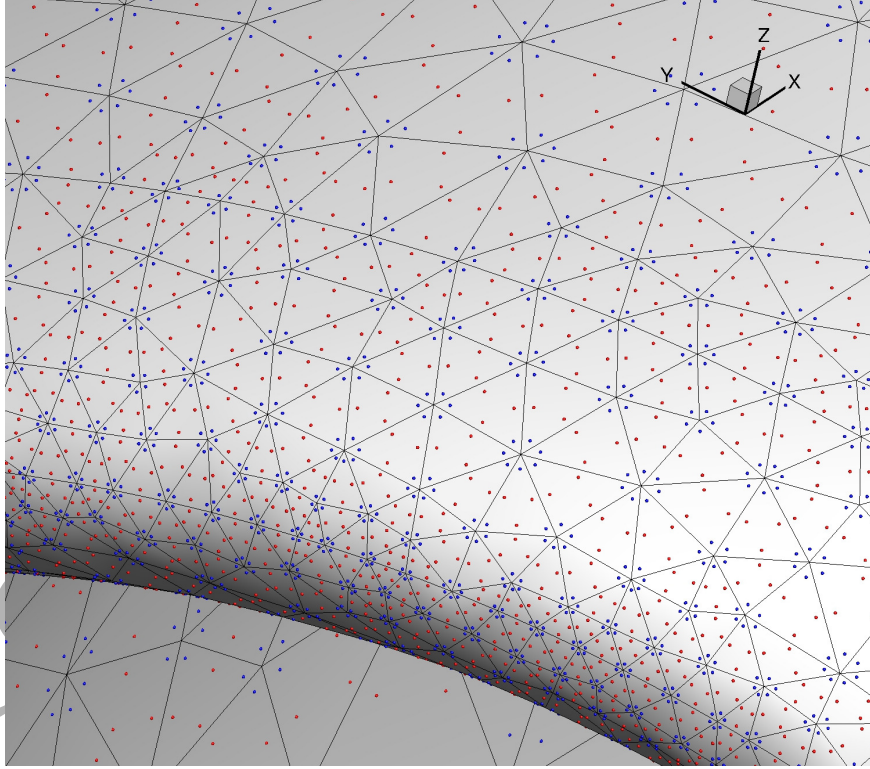

Figure 1: Close-up of the surface mesh and the corresponding quadrature points for a WENO third-order scheme, colour codes according to their corresponding weight value.

The weight and distribution of the quadrature points depend upon the order of the Gaussian quadrature rule employed, higher integration rule will result in enhanced interface flux approximation. The convective

7

and viscous flux tensors are defined as:

$$\mathbf{F}_c^{\mathbf{n,l}} = F_c^{\mathbf{x}} n_x + F_c^{\mathbf{y}} n_y + F_c^{\mathbf{z}} n_z,$$
$$\mathbf{F}_v^{\mathbf{n,l}} = F_v^{\mathbf{x}} n_x + F_v^{\mathbf{y}} n_y + F_v^{\mathbf{z}} n_z,$$
(11)

where n_x, n_y and n_z are the Cartesian components of the normal vector on the inter-element surface. The interface fluxes are computed from the reconstructed solution which is extrapolated at the interface. The solution is reconstructed from element-averaged data. The following section describe the methodology adopted for the reconstruction procedure.

3.1. Spatial Discretisation

The main objective of the reconstruction process is to build a high-order polynomial $p_i(x, y, z)$ of arbitrary order r, for each considered element V_i that has the same average as a general quantity $\mathbf{U}_i$ [43]. This can be formulated as

$$\mathbf{U}_i = \frac{1}{|V_i|} \int_{V_i} \mathbf{U}(x, y, z) \, dV = \frac{1}{|V_i|} \int_{V_i} p_i(x, y, z) \, dV.$$
(12)

The reconstruction method is based on the approach of [3, 23], and only the key details are highlighted in this paper. The reconstruction is carried out in a transformed system of coordinates in order to minimize scaling effects that appear in stencils consisting of elements of different size as well as to improve the condition number of the system of equations [3, 23, 44]. The transformation is achieved by decomposing each element into tetrahedrals. Since a transformation based on shape functions of elements can fail when non-planar faces are encountered, this also applies to the quadrilateral faces, which need to be decomposed to triangular ones in order to accurately compute the normal vectors [3]. The reconstruction polynomial at the transformed element V_i' is expanded over local polynomial basis functions labelled as $\phi_k(\xi, \eta, \zeta)$, which are given by:

$$p(\xi, \eta, \zeta) = \sum_{k=0}^{K} a_k \phi_k(\xi, \eta, \zeta) = \mathbf{U}_0 + \sum_{k=1}^{K} a_k \phi_k(\xi, \eta, \zeta),$$
(13)

where ξ, η, ζ are the coordinates in the reference system, a_k are the degrees of freedom and the upper index in the summation of expansion. K is related to the order of the polynomial r by $K = \frac{1}{6}(r+1)(r+2)(r+3) - 1$. It must be stressed that the decomposition to tetrahedrals, is carried out to improve the condition of the reconstruction matrices only, rather than computing inter-element variables e.g. fluxes, since the use of prismatic or hexahedral elements for the boundary layer region is beneficial for computing the gradients with high-accuracy. For computing the degrees of freedom a_k, a minimum of K elements is required in the stencil in addition to the target element. Using the minimum possible number of elements in the stencil, $M \equiv K$, may produce ill-conditioned systems, hence using $M = 2 \cdot K$ improves the robustness of the method

8

as described in [23, 44]. A linear least-square method is adopted to enable the system of equations of (13) for the unknown degrees of freedom a_k. The final form of the linear system is solve with the QR decomposition algorithm. Discontinuous solutions are often encounter in external aerodynamics, thus limiting functions are essential for maintaining numerical stability and suppress any spurious oscillations. Two approaches are assessed in this work the MUSCL and the WENO schemes.

3.1.1. MUSCL

The MUSCL scheme employed in this work is based on the Barth and Jespersen slope limiter [45]. The design of the scheme requires the minimum and maximum values in the stencil's neighbourhood, i.e., $U_i^{min} = \min(U_i, U_l)$ and $U_i^{max} = \max(U_i, U_l)$, where $l = 1, ..L$; L is the total number neighbours of element i. The gradient of a general quantity is defined as ∇U_i and is an approximation of the solution gradient inside the element i. The gradient is computed during the reconstruction process by incorporating information from the entire central stencil. The scheme is written as

$$U_{i\alpha} = U_i^c + \phi_i \nabla U_i \cdot x_\alpha, \tag{14}$$

where U_i^c is the value for the general quantity at the element centroid and x_α are the coordinates of the quadrature point. The limiter seeks the minimum value of the slope limiter for all the quadrature points that satisfy conditions: $\phi_i = \min(\phi_{i,m_1}, \phi_{i,m_2}, ...\phi_{i,M})$. Then, the limiting function is applied, composed by three different states according to the difference of the reconstructed value at the quadrature points of the considered element $U_{(i,\alpha)}$, the minimum and maximum values from the neighbours U_l, and the element centre value U_i, yielding:

$$\phi_{i,\alpha} = \begin{cases} \min\left(1, \dfrac{U_i^{max} - U_i}{U_{i,\alpha} - U_i}\right), & \text{if } U_{i,\alpha} - U_i > 0 \\ \min\left(1, \dfrac{U_i^{min} - U_i}{U_{i,\alpha} - U_i}\right), & \text{if } U_{i,\alpha} - U_i < 0 \\ 1, & \text{if } U_{i,\alpha} - U_i = 0. \end{cases} \tag{15}$$

3.1.2. WENO

WENO schemes use a non-linear combination of various reconstruction polynomials, where each polynomial is weighted according to the smoothness of its solution. The polynomials are given by

$$p_i^{\text{weno}} = \sum_{m=1}^{m_s} \omega_m p_m(\xi, \eta, \zeta), \tag{16}$$

9

where m_s is the total number of WENO stencils. Substituting back to equation (13) for $p_m(\xi, \eta, \zeta)$, we obtain the following expression

$$p_m(\xi, \eta, \zeta) = \sum_{m=0}^{K} a_k^{(m)} \phi_k(\xi, \eta, \zeta). \tag{17}$$

Using the condition that the sum of all weights is unity, yields

$$p_i^{\text{weno}} = \mathbf{U}_0 + \sum_{k=1}^{K} \left(\sum_{m=0}^{m_s} \omega_m a_k^m \right) \phi_k(\xi, \eta, \zeta) \equiv \mathbf{U}_0 + \sum_{k=1}^{K} \tilde{a}_k \phi_k(\xi, \eta, \zeta), \tag{18}$$

where $\tilde{a}_k$ are the reconstructed degrees of freedom; and the non-linear weight ω_m as

$$\omega_m = \frac{\tilde{\omega}_m}{\sum\limits_{m=0}^{m_s} \tilde{\omega}_m} \quad \text{where} \quad \tilde{\omega}_m = \frac{\lambda_m}{(\epsilon + \mathcal{I}_m)^b}. \tag{19}$$

The smoothness indicator is given by

$$\mathcal{I}_m = \sum_{1 \leq |\beta| \leq r} \int_{\tilde{E}_i} \left(\mathcal{D}^\beta p_m(\xi, \eta, \zeta) \right)^2 (d\xi, d\eta, d\zeta), \tag{20}$$

where β is a multi-index, r is the polynomial's order, λ_m is the linear weight, and D is the derivative operator. The smoothness indicator is a quadratic function of the degrees of freedom (a_k^m) and can be expressed as a universal mesh-independent oscillation indicator matrix.

The various reconstruction polynomials arise from different sets of stencils that satisfy some geometrical conditions. The reader is referred to [3, 23, 44], and references therein, for a comprehensive explanation of the different set of geometrical conditions and WENO characteristic reconstruction.

Additionally for the MUSCL and WENO schemes for ensuring that the pressure and density remain positive through the reconstruction the positivity condition of [13] is used where the reconstructed values of density and pressure for each Gaussian quadrature points (α) must satisfy the following condition:

$$|\rho_{i\alpha} - \rho_i| < 0.8\rho_i \quad and \quad |p_{i\alpha} - p_i| < 0.8p_i. \tag{21}$$

If the condition (21) is not satisfied for all Gaussian quadrature points then the reconstruction order for the considered element is reduced by one order until the condition is satisfied.

3.2. Fluxes Approximation

Having reconstructed the element-averaged solutions, the interface fluxes can be evaluated. For the convective fluxes the Riemann problem is solved with the approximate Harten-Lax-van Leer-Contact (HLLC) solver as proposed in [46]. The HLLC solver is also employed for the convective part of the turbulence transport equation when a higher than first-order discretisation of the turbulence variable is adopted. The

10

HLLC flux function is given as:

$$
\hat{\mathrm{F}}^{\mathbf{HLLC}} \begin{cases} \hat{F}^-, & \text{if } 0 \leq S^-, \\ \hat{F}^{*-} = \hat{F}^- + S^- \left(\hat{W}^{*-} - \hat{W}^- \right), & \text{if } S^- \leq 0 \leq S^*, \\ \hat{F}^{*+} = \hat{F}^+ + S^+ \left(\hat{W}^{*+} - \hat{W}^+ \right), & \text{if } S^* \leq 0 \leq S^+, \\ \hat{F}^+, & \text{if } 0 \geq S^+, \end{cases} \tag{22}
$$

where

$$
\hat{W}^{*\pm} = \rho^\pm \left(\frac{S^\pm - u^\pm}{S^\pm - S^*} \right) \begin{bmatrix} 1 \\ S^* \\ v^\pm \\ w^\pm \\ \frac{E^\pm}{\rho^\pm} (S^* - u^\pm) \left(S^* + \frac{p^\pm}{\rho^\pm (S^\pm - u^\pm)} \right) \\ \frac{\tilde{\nu}}{\rho^\pm} \end{bmatrix}. \tag{23}
$$

$\hat{W}^{*\pm}$ is computed either for the considered element "$-$", or for its neighbour "$+$" and the wave speeds $+S^-, +S^+, S^*$ are approximated by an adaptive iterative procedure as detailed in [46].

The discretisation of the convective turbulence flux term has significant impact on the amount of artificial dissipation produced by the turbulence model. Disproportional amounts of eddy viscosity are introduced when there is a severe mismatch between the discretisation of the mean flow and turbulence model equations. Mispredictions of eddy viscosity production can lead to very small or negative values. Several numerical experiments were performed in order to establish the most stable and accurate methodology for the discretisation of the turbulence model terms, including the convective component, the turbulence model variable gradients and source terms which are depended upon the velocity, turbulence model gradients. For second-order mean flow discretisation, a first-order upwind flux is employed for the turbulence model convective term and the second-order scheme for all gradients. The convective turbulent flux $\hat{F}_c^{\tilde{\nu}}$ for a second-order scheme is computed as

$$
\hat{F}_c^{\tilde{\nu}} = \frac{1}{2} \left[\mathcal{N} \left((\tilde{\nu})^- + (\tilde{\nu})^+ \right) - |\mathcal{N}| \left((\tilde{\nu})^+ - (\tilde{\nu})^- \right) \right], \tag{24}
$$

where $(\nu)^-$ and $(\nu)^+$ are the element-centred values of the turbulent eddy viscosity for the considered element and its direct side neighbour, respectively, with $\mathcal{N}$ defined as

$$
\mathcal{N} = \frac{1}{2} \left[n_x \left(u^- + u^+ \right) + n_y \left(v^- + v^+ \right) + n_z \left(w^- + w^+ \right) \right], \tag{25}
$$

where $u^\pm$, $v^\pm$, $w^\pm$ are the element-centred values of the Cartesian velocity components.

11

For high-order mean flow discretisation it was found that the most stable method with accurate solutions, is to treat the turbulence convective term through the Riemann solver as shown in equation (23). The turbulence model variable is reconstructed according to the high-order spatial scheme of the mean flow equations either with a MUSCL or WENO approach whereas the gradients are estimated with the same approach as viscous terms. For the evaluation of the viscous fluxes the extrapolated interface variables $U_{i,a}^{\pm}$ and their unlimited gradients $\nabla U_{i,a}^{\pm}$ from the k-exact least square reconstruction of equation (12) are averaged from two discontinuous states as detailed in [3, 47]. Although, other methods for the evaluation of the diffusive fluxes such as the one of the generalised Riemann problem of Gassner et al. [48], or the diffusive flux of direct DG [49, 50] can be applied, the k-order accurate flux is implemented as it easily obtained through element centred reconstructions and has been applied for various flows problems [47, 51, 52].

This k-exact reconstruction flux approximation has been previously assessed by Ivan and Groth [47] and it is not susceptible to odd-even decoupling, however the discrete maximum principle is not satisfied and is influenced by the mesh quality, which agrees with the rule that for finite volume discretisation methods, accuracy and positivity are conflicting properties. Therefore, for stability purposes, and when dealing with meshes consisting of non-planar quadrilateral faces, hence poor quality hexahedral, prisms and pyramids, the least square reconstruction can introduce severe errors in the computation of the viscous flux gradients. As it has been reported by Diskin et al [53], where extensive tests have been performed for different grid topologies with high aspect ratio and skewness elements, the Green-Gauss formulation for computing the viscous terms is much more robust and less sensitive to the quality of the grid element.

In the presence low radius curvature (e.g. leading edge of a wing) highly skewed elements can introduce large errors when computing their gradients with a least square reconstruction of high-order polynomial. Therefore, for each element that has an aspect-ratio greater than a threshold value ≈ 100, we utilise the Green-Gauss formulation as described in [3], otherwise the least square reconstruction procedure for the gradients is employed. This condition of gradient approximation is only applicable to the gradients of the viscous terms. In the convective terms, the least square reconstruction is used both with the MUSCL and WENO schemes.

3.3. Low-Mach Number Treatment Modification

A low-Mach number modification is employed in the present study for subsonic flows and it follows the previous work of Thornber et al. [32], where the left and right state of the reconstructed velocities, **normal** to the interface are modified in a linear way with respect to the local Mach number. In the case of the local

speed approaches to zero the arithmetic mean of them is modified in the following manner:

$$u_L^* = \frac{(1+\zeta)u_L + (1-\zeta)u_R}{2}, \quad u_R^* = \frac{(1+\zeta)u_R + (1-\zeta)u_L}{2}, \tag{26}$$

with the function ζ being equal to $\zeta = min(1, max(M_L, M_R))$. The Mach number for the left and right states are calculated based on the velocity magnitude of all the velocity components independent of the normal direction in which the flux is computed. This modification is different in nature from a preconditioning step used for changing the flow variables, since our main motivation is not to relax the restriction in terms of the time-step size, but rather to increase the resolution at low speed regions, where this modification has demonstrated increased resolution and accuracy for a wide-range of flow problems [1, 2, 32, 33, 54], can be utilised with any Riemann solver and without computational overheads.

3.4. Time discretisation

Convergence to steady state solution are obtained with the lower-upper symmetric Gauss-Seidel (LU-SGS) implicit time integration method in conjunction with local time stepping algorithm. The LU scheme was introduced by Jameson [55] and it is extensively used for high-Reynolds number flows on unstructured grids [56–61] in various formulations including WENO and Spectral schemes. Although, alternative implicit-time stepping methods are introduced for unstructured grids e.g. the Newton-Krylov GMRES implementations [62], the present time advancement scheme is considered to be robust with efficient parallelisation and low computational cost. The LU-SGS scheme with an approximate first-order Jacobian is considered. Equation (10) can be rewritten in the following semi-discrete form

$$\frac{d\mathbf{U}_i}{dt} = \mathbf{R}_i, \tag{27}$$

where $\mathbf{R}_i$ is the right-hand side residual, which should converge to the machine precision. Employing a first-order backward Euler implicit time stepping scheme, equation (27) takes the following form

$$\frac{d\mathbf{U}_i^n}{dt} = \frac{\mathbf{U}_i^{n+1} - \mathbf{U}_i^n}{dt} = \mathbf{R}_i^{n+1}. \tag{28}$$

Linearising in time, equation (28) gives

$$\frac{d\mathbf{U}_i^n}{dt} = \mathbf{R}_i^n + \frac{\partial \mathbf{R}_i^n}{\partial \mathbf{U}}, \tag{29}$$

where $\mathbf{R}_i$ should be equal to zero, hence equation (29) becomes

$$\left(\frac{\mathbf{I}}{dt} - \frac{\partial \mathbf{R}_i^n}{\partial \mathbf{U}} \right) d\mathbf{U}_i = \mathbf{R}_i^n. \tag{30}$$

13

The solution at each element i is updated as $\mathbf{U}_i^{n+1} = \mathbf{U}_i^n + d\mathbf{U}_i$, where $\mathbf{I}$ stands for the identity matrix. The term $\frac{\partial \mathbf{R}_i^n}{\partial \mathbf{U}}$ is the Jacobian matrix and contains the linearisation of the inviscid and viscous flux vectors as well as the source terms. For obtaining the quadratic convergence properties of the Newton's method, the linearisation of the numerical flux function must be exact. However the formulation of the exact Jacobian matrices for high-order non-linear schemes such as WENO methods, require excessive memory storage [41, 63]. Since we are only interested in steady state solutions and in order to simplify the linearisation of the Jacobian, a first-order approximation of the numerical fluxes is employed, since the matrix of $\frac{\partial \mathbf{R}_i^n}{\partial \mathbf{U}}$ is identical to the graph of the corresponding unstructured grid. The numerical flux is estimated with the Rusanov flux function given as

$$\mathbf{R}_i\left(\mathbf{U}_i, \mathbf{U}_j, n_{ij}\right) = \frac{1}{2}\left(\mathbf{F}_{\mathbf{c},\mathbf{v}}^{\mathbf{n_{ij}}}(\mathbf{U}_i, \nabla \mathbf{U}_i) + \mathbf{F}_{\mathbf{c},\mathbf{v}}^{\mathbf{n_{ij}}}(\mathbf{U}_j, \nabla \mathbf{U}_j)\right) - \frac{1}{2}|\lambda_c^{ij} + \lambda_v^{ij}|(\mathbf{U}_j - \mathbf{U}_i), \tag{31}$$

with the maximum convective and viscous eigenvalue written respectively

$$\lambda_c^{ij} = |\mathbf{V}_{ij} \cdot \mathbf{n}_{ij}| + a_{ij}, \quad \lambda_v^{ij} = \frac{\mu_{ij}}{\rho_{ij}|x_j - x_i|}, \tag{32}$$

where $\mathbf{n}_{ij}$ is the normal vector to the element interface, $\mathbf{V}_{ij}$ is the velocity vector and a_{ij} is the speed of sound. The viscous eigenvalue is approximated by the viscous spectral radius $x_j - x_i$ of the element barycenter. Linearising the Rusanov flux of equation (31) gives the diagonal and off-diagonal components respectively:

$$\begin{aligned}
\frac{\partial \mathbf{R}_i}{\partial \mathbf{U}_i} &= \frac{1}{2}\left(\frac{\partial \mathbf{F}_{c,v}}{\partial \mathbf{U}_i} + |\lambda_c^{ij} + \lambda_v^{ij}|\mathbf{I}\right), \\
\frac{\partial \mathbf{R}_i}{\partial \mathbf{U}_j} &= \frac{1}{2}\left(\frac{\partial \mathbf{F}_{c,v}}{\partial \mathbf{U}_j} - |\lambda_c^{ij} + \lambda_v^{ij}|\mathbf{I}\right).
\end{aligned} \tag{33}$$

Due to these approximations, the quadratic convergence of the Newton's method will not be achieved due to the discrepancy in the resolution of the right- and left-hand sides of equation (30). The resulting linear system of the form $AX = B$ of equation (30), following the implementation of [58], is solved by a two step approach, consisting of two sweeps; the forward and backward sweeps are given by the following two equations upper and lower part, respectively:

$$(D + L)\, d\mathbf{U}^* = \mathbf{R}\,(D + U)\, d\mathbf{U} = D d\mathbf{U}^*. \tag{34}$$

14

Where $\mathbf{U}^*$ is the intermediate state, the upper, lower and diagonal components of the system of equations are written as

$$
\begin{aligned}
U &= \frac{1}{2}\left(\frac{\partial \mathbf{F}_{c,v}}{\partial \mathbf{U}_i} - |\lambda_c^{ij} + \lambda_v^{ij}|\mathbf{I}\right), \\
L &= \frac{1}{2}\left(-\frac{\partial \mathbf{F}_{c,v}}{\partial \mathbf{U}_j} - |\lambda_c^{ij} + \lambda_v^{ij}|\mathbf{I}\right), \\
D &= \frac{\mathbf{I}}{dt} + \sum_{l=1}^{N_f}\frac{1}{2}\left(\frac{\partial \mathbf{F}_{c,v}}{\partial \mathbf{U}_i} + |\lambda_c^{ij} + \lambda_v^{ij}|\mathbf{I}\right) - \frac{\partial \mathbf{S}}{\partial \mathbf{U}}.
\end{aligned}
\tag{35}
$$

The implicit scheme has small computational cost per iteration and the only storage requirements arise from the diagonal of the equation above. The diagonal elements of the matrix must be stored and inverted directly and the off-diagonal ones are computed at every stage. Hence, the diagonal elements used in the present study are scalars multiplied by the identity matrix and the off-diagonals are computed according to equation (33). The number of sweeps per Newton iteration is set to 5 in the present study, based on the findings of various approaches using the LU-SGS schemes for similar flow problems [56–61]. The source term $\mathbf{S}$ is differentiated with respect to the turbulence model variable only, in order to keep the diagonal dominance of the system matrix, and the source term Jacobian is restricted to be positive as suggested by [42], hence

$$
\frac{d\mathbf{S}}{d\tilde{\nu}} = C_{b1}\tilde{S} + \frac{1}{\sigma}C_{b2}2\left(\nabla\tilde{\nu}\right) - 2C_{w1}f_w\left(\frac{\tilde{\nu}}{d^2}\right) \leq 0.
\tag{36}
$$

Finally, the boundary conditions are also treated implicitly according to Batten et al. [63].

4. Results and Discussion

Computations are performed for three two-dimensional and three three-dimensional external aerodynamic flows of aeronautical configurations. The MUSCL second- and third-order schemes and the WENO third- and fifth-order schemes are employed, henceforth labelled as M2, M3, W3 and W5, respectively. The MUSCL schemes of higher-order of accuracy are not pursued since due to their non-differentiable nature of the limiters they can not achieve higher-order of accuracy. The W3 scheme has a desirable balance between accuracy and computational cost, whereas the W5 is significantly more expensive. High-order discretisation of turbulence model variable in a coupled fashion is extensively assessed and presented for some representative case. The low-Mach number treatment technique is investigated and the findings are presented with main focus on flows with regions of low velocity. Three types of boundary conditions are implemented, no-slip wall for all body surfaces, characteristics based far-field boundary conditions and where appropriate symmetry conditions. The flow cases are presented in an escalating level in terms of difficulty, complexity

15

and overall computational effort. Grid convergence study is performed for all cases excluding the flow over the DLR-F11 aircraft configuration due to computational budgets available. Grid refinement strategy follows the simple rule of halving the element size on the wall surface; the strategy is applied in regions of interest i.e. near boundary layers, shocks and wakes. Computations are performed without wall-functions thus y+ values are kept to unity.

4.1. NACA-0012

The first case concerns the subsonic turbulent flow around the symmetric NACA-0012 aerofoil at zero degree incidence. Freestream conditions correspond a Mach number of $M_\infty = 0.3$, angle of attack of $\alpha = 0°$ and a Reynolds number of $Re_c = 1.85 \times 10^6$ based on the aerofoil chord length. Five grids are generated, the grid statistics are shown in table 1. A hyperbolic method is employed for the inflation of the quadrilateral layer with a constant growth rate of 1.1; figure 2 shows a close-up of the coarse grid topology. The aim of this test case is to evaluate the benefit of high-order reconstruction methodology for RANS solutions on fully attached flow over symmetric aerofoils.
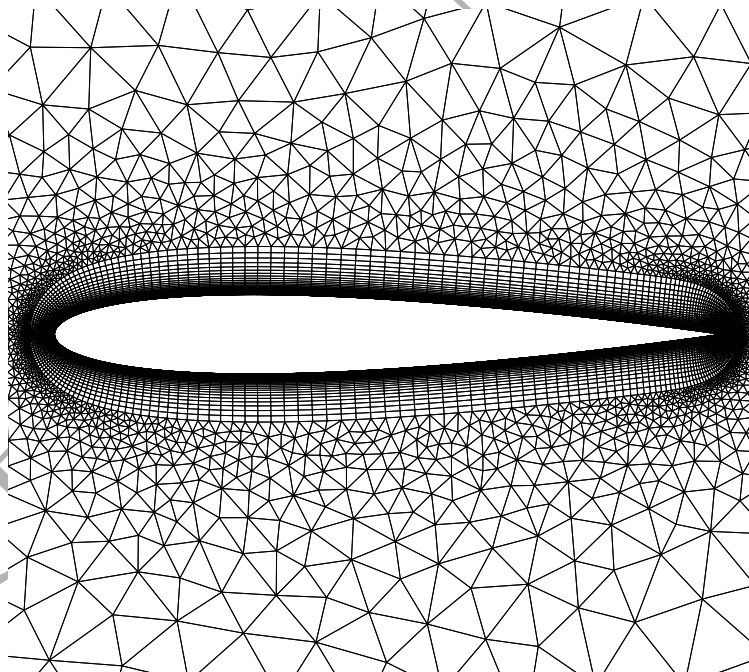
Figure 2: Close-up of the coarse grid for the NACA-0012 aerofoil.

With respect to convergence properties the solutions of order smaller than fifth exhibit a residual drop of at least eight orders of magnitude, where the fifth order solution suggests a plateau at 10^{-7}, this is also reported by Yang et al in 2009 [17] for the WENO 5th order solution over a wing. The residual trends

16

Table 1: Grid properties for the NACA-0012 test case.

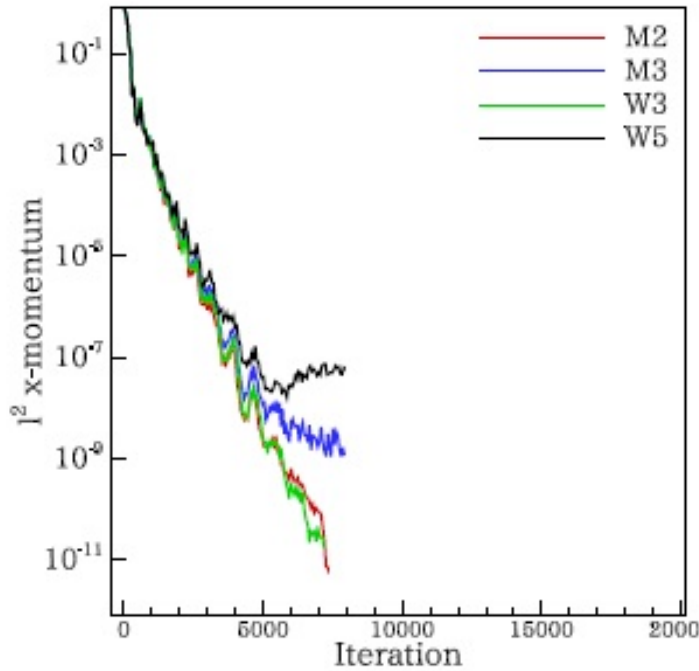|	Super-Coarse	Coarse	Medium	Fine	Super-Fine
Elements	6,257	11,264	20,803	41,710	87,597
Aerofoil points	73	148	299	597	1,193
y+	1.0	0.8	0.6	0.5	0.5

Figure 3: Residuals for l^2 norms of x-momentum for the subsonic flow over the NACA-0012 aerofoil on the fine grid ($M_\infty = 0.3$ $\alpha = 0°$ and $Re_c = 1.85 \times 10^6$).

are depicted in figure 3 where the l^2 norms of x-momentum (ρu) on the super-fine grid are plotted for the MUSCL and WENO solutions of second and third, and third and fifth order, respectively. It is worth mentioning that the convergence rate is similar for all spatial schemes including the conserved variables and turbulence parameter ($\rho, \rho u, \rho v, E, \mu$) up until $5,000$ iterations and no considerable grid dependence is observed with respect to either the speed or the convergence levels.

In terms of accuracy, the pressure coefficient (C_p) estimates are shown in figure 4 and compared with the experimental data obtained from the AGARD report [64]. This case is characterised by a smooth attached flow throughout the surface of the aerofoil, which is also predicted by the computed solutions, leading to good agreement with the experiment. There are no apparent differences in the C_p profiles for all numerical schemes on the fine grid, however there are variations in the drag prediction.

Figure 5 shows the relative error of coefficient of drag for all numerical schemes and grids, plotted against the wall-clock time. The relative drag error is computed based on an additional refinement M2 solution,
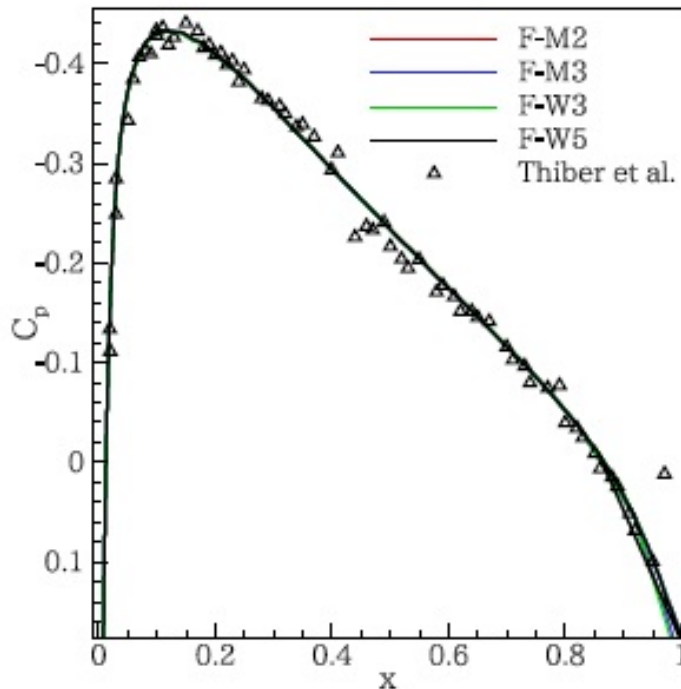
17

Figure 4: Pressure coefficient (C_p) on the fine grid for the NACA-0012 case compared with experiment data [64] ($M_\infty = 0.3$ $\alpha = 0°$ and $Re_c = 1.85 \times 10^6$).

where the indicative wall clock time is based on the computations performed on a intel-i7 3820 four core processor. Each line corresponds to one numerical scheme for the five grid refinements, starting from the left hand side with the coarse one. Only WENO predictions can reach lower than 10^-4 error levels for the given grids. W5 solutions demonstrate higher error for the same spatial refinement compared with the W3, this may be attributed to the higher grid quality requirements of the stencil construction in terms of smoothness and isotropy for the fifth order scheme compared with the third-order one. Additionally, the imbalance in the resolution between the left and right hand side of the implicit time-stepping due to the first-order Jacobian approximation could also be responsible for this behaviour. It has to be noted, that for the super-coarse and coarse grids the average aspect ratio in the vicinity of the aerofoil surface is around $5,000$.

4.2. RAE-2822

The shock capturing capabilities of the numerical framework are assessed with the two-dimensional transonic flow around the RAE-2822 supercritical aerofoil. The freestream conditions are based on the wind tunnel measurements performed in 1979 and presented in the technical report by Cook et al. [65]. Case 6 is investigated where the wind tunnel freestream conditions correspond to a Mach number of $M_\infty = 0.725$,
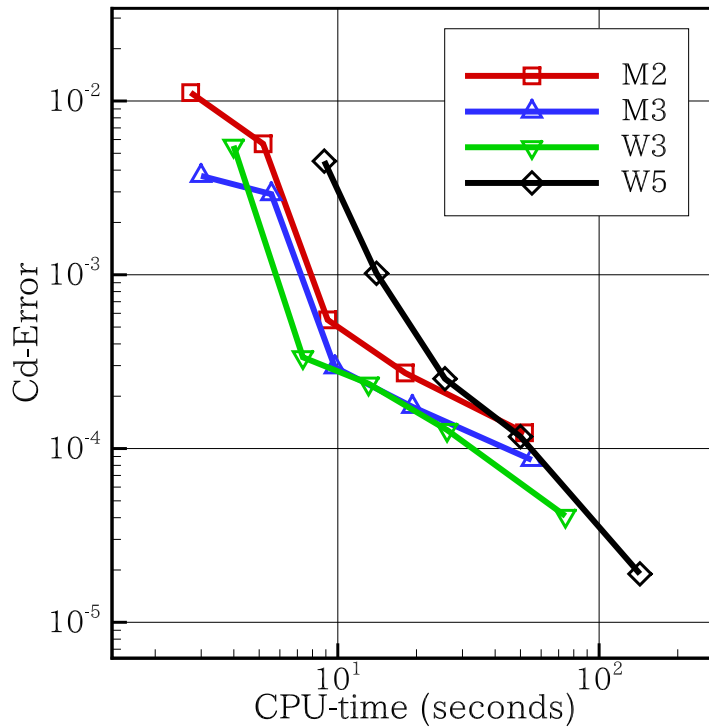
18

Figure 5: Relative drag error against wall-clock time in seconds on an i7-3820 processor for the NACA-0012 case ($M_\infty = 0.3$ $\alpha = 0°$ and $Re_c = 1.85 \times 10^6$).

an angle of incidence of $\alpha = 2.92°$ and Reynolds number based on the aerofoil chord of $Re_c = 6.5 \times 10^6$. Several modifications on the Mach number and angle of attack have been proposed in order to account for wall interference. The corrected Mach number of $M_\infty = 0.729$, angle of attack of $\alpha = 2.31°$ and with the same Reynolds number are adopted for the current analysis as performed also in [66].

The outer boundary is positioned approximately 100 chord lengths away from the aerofoil to minimize any artificial reflections from the outer boundary conditions. The flow is characterised by a normal shock on the upper surface of the aerofoil interacting with the boundary layer, which considerably thickens downstream up to the end of the trailing edge. To account for the shock-wave boundary layer interaction on the suction side and benefit of the flexibility of unstructured grids a non-uniform distribution of points is set for the upper and lower part of the aerofoil. Three hybrid unstructured grids are generated their details are tabulated in table 2, the meshes are generated based on the o-grid strategy, the coarse grid is shown in figure 6.

High-order discretisation of turbulence model poses robustness and accuracy challenges for the RANS computations. Negative values of eddy viscosity in the vicinity of the boundary layer edge as well as non-physical oscillations are often encountered in high Reynolds number flows with high-order approximations particularly for under-resolved grids [38, 67, 68]. The effect of discretisation of the turbulence parameter for
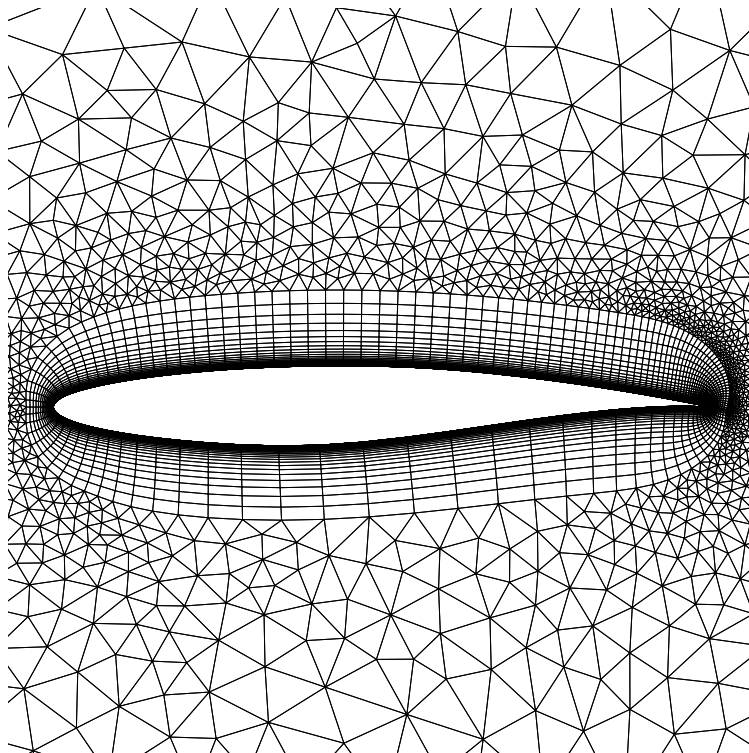
19

Figure 6: Coarse grid for the RAE-2822 case.

Table 2: Grid properties for the RAE-2822 test case.

	Coarse	Medium	Fine
Elements	10,714	23,852	51,294
Upper surface points	85	170	341
Lower surface points	45	90	188
y+	1.0	0.8	0.6

high-order reconstruction is presented for this case in terms of accuracy and convergence. Figure 7 depicts

the residual histories on the fine grid for the second, third and fifth order schemes, where the coupled (COU)

approach refers to a discretisation of the turbulence parameter according to the type (WENO or MUSCL)

and order of the mean flow variable approximation, whereas the decoupled refers to a discretisation of the

turbulence parameter according to a first order upwind method, shown in equation (24). The residual

histories suggest that for the third and fifth order coupled results, a lower drop than the decoupled ones is

achieved. However, this is not the case for the second order solution, which could be attributed to the non-

differentiable nature of the slope limiter used for the turbulence model variable that in turn influences the

mean flow residuals. The two discretisation approaches differ also on the level of eddy viscosity production,

particularly for the higher-order solutions, this is illustrated in figure 8 for the WENO third order solution

20
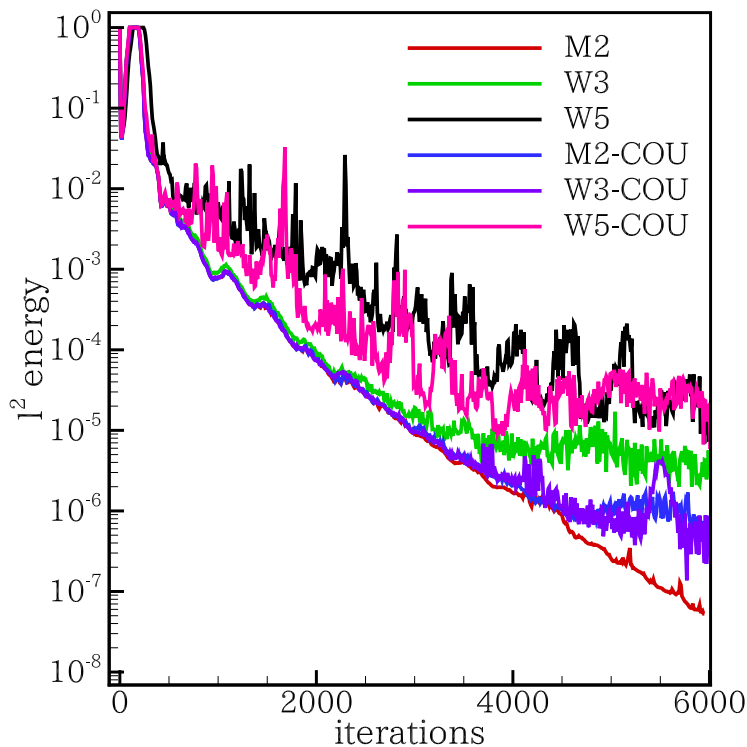
Figure 7: Residual histories of l^2 norm for total energy for the RAE-2822 aerofoil ($M_\infty = 0.729$, $\alpha = 2.31°$ and $Re_c = 6.5 \times 10^6$).

on the fine grid.

In terms of accuracy the coupled approach for higher than third order discretisation is shown in figure 9 where the relative drag coefficient is plotted against grid refinement defined as $h = 1/\sqrt{Elements}$. The benefit of discretising the turbulence parameter according to the mean flow equation method is amplified with higher grid resolution for the WENO method, where the MUSCL type solution suggest small differences between the coupled and decoupled approach. This effect is also demonstrated in figure 10, where the coefficient of pressure on the coarse grid is compared against the fine fifth order solution and the experimental data of Cook et al. [65]. Henceforth all solutions presented in this work correspond to the coupled method for higher than second order schemes and only for the second order solutions a decoupled manner is adopted including the NACA-0012 case.

4.3. MDA 30P-30N

Flow phenomena around high-lift devices are considered challenging for numerical methods and turbulence model discretisation; deployed slat and flap at high angles of attack in combination with low speed, potential unsteady flow regime, flow separation, laminar/turbulent transition, interaction of aerofoil/wing elements, streamline curvature, wake in pressure gradient are some of the them. A well established case for
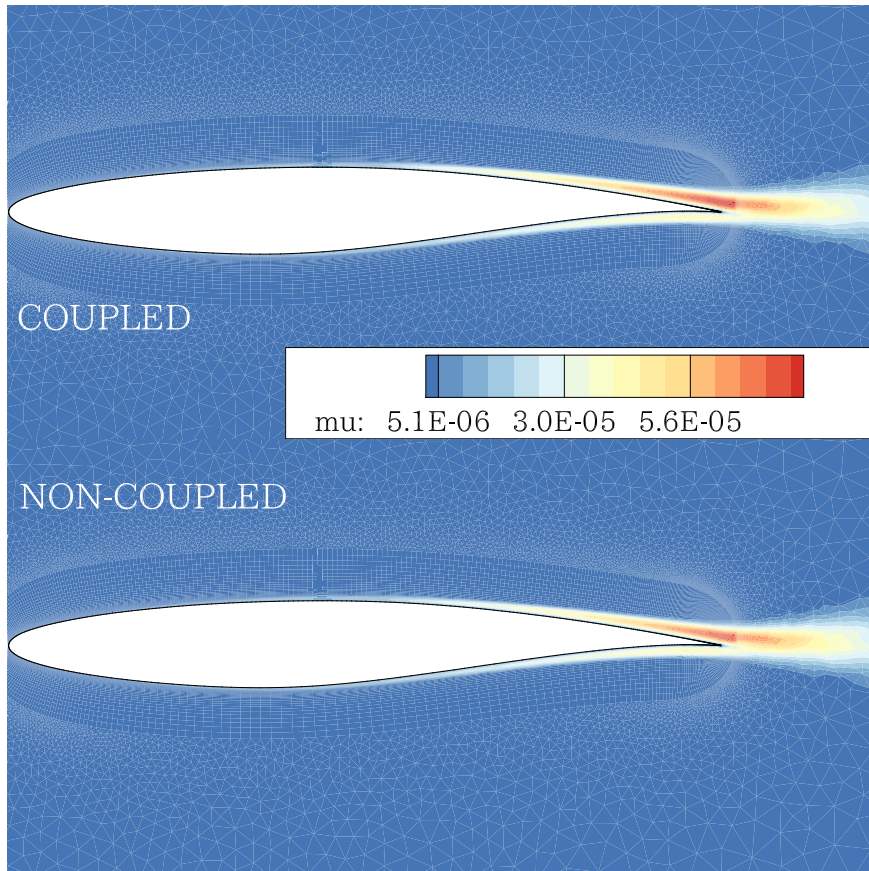
21

Figure 8: Eddy viscosity production for the coupled and decoupled approaches on the WENO third order fine grid for the RAE-2822 aerofoil ($M_\infty = 0.729$, $\alpha = 2.31°$ and $Re_c = 6.5 \times 10^6$).

assessing the performance and accuracy of the developed numerical framework for flow over high-lift devices is the McDonnell Douglas three-element configuration at 30P-30N or simply MDA 30P-30N. The freestream conditions correspond to a Mach number of $M_\infty = 0.2$, an angle of incidence of $\alpha = 16°$ and Reynolds number based on the reference aerofoil chord length of $Re_c = 9 \times 10^6$. The flow around this configuration has been previously studied experimentally by Spaid [69] and by Rumsey et al [70], where 3D effects are analysed including CFD simulations, further CFD work is presented in the following papers [71–74].

Three hybrid unstructured grids are generated, labelled as coarse, medium and fine the grid properties are presented in table 3 where the grid topology is visualised in figure 11 for the medium grid. The grid is locally refined around the aerofoil elements and the wake.

The flow over the high lift aerofoil is characterised by several low speed regions i.e. at the lower surface of the slat and inside the slot with the sharp corner cove. Compressible solvers inherently struggle with low speed flow regions, due to the stiffness of the system of equations, leading to slow convergence rates and
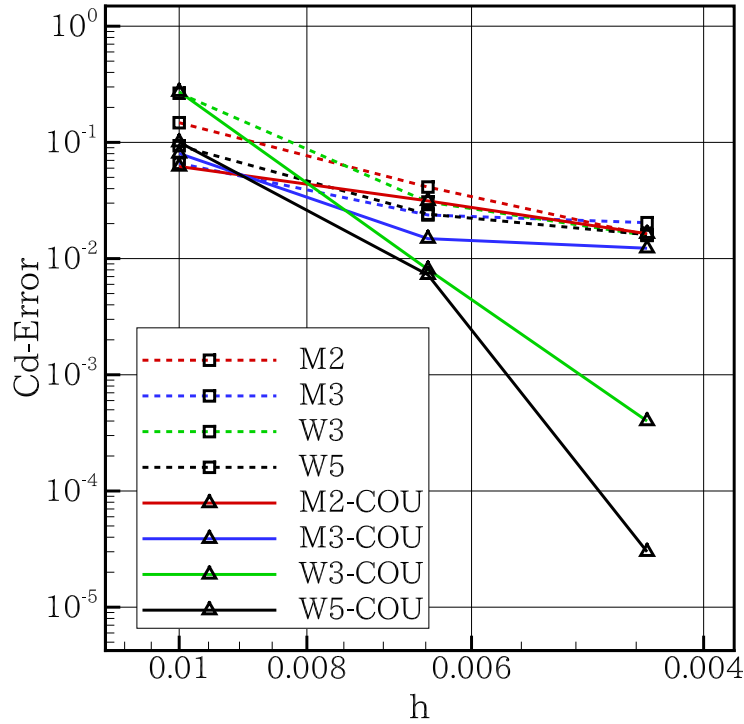
Figure 9: Relative drag coefficient error for different grid for the RAE-2822 aerofoil ($M_\infty = 0.729$, $\alpha = 2.31°$ and $Re_c = 6.5 \times 10^6$).

Table 3: Grid proprerties for the MDA-30P-30N aerofoil.

	Coarse	Medium	Fine
Elements	34,184	74,902	192,845
Slat points	90	147	284
Main element points	203	372	667
Flap points	85	140	265
y+	1.0	0.8	0.6

impaired accuracy. To surpass the accuracy challenge the low-Mach number treatment method presented in the previous section is investigated. Simulations are performed with the second and third order MUSCL scheme as well as with the third and fifth order WENO, with and without the low-Mach number (LM) treatment. The benefit of the low-Mach number treatment in terms of flow structures is most evident in low speed regions, predicting an accurate representation of the flow, illustrated in figure 13 where Mach number contours are plotted, overlaid with streamlines on the medium grid W3 solutions. The LM treatment effect is also mirrored on the increased eddy viscosity production near low velocity regions, depicted in figure 12 where the eddy viscosity is plotted on the medium grid W3 solutions, whereas near the wake, lower amounts of eddy viscosity are observed.
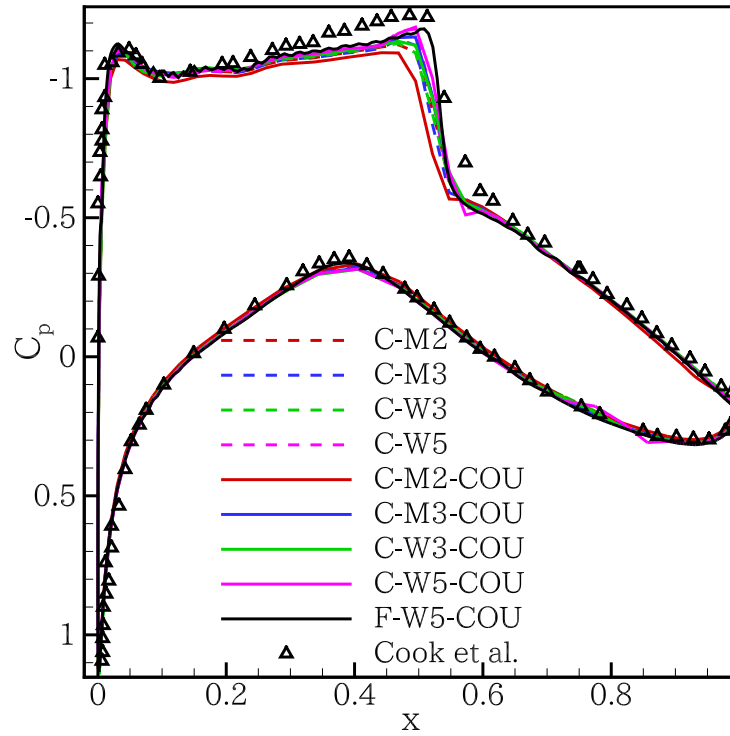
23

Figure 10: Coefficient of pressure (C_p) variations for the coupled and decoupled approaches on the RAE-2822 aerofoil compared with the experimental data [65] ($M_\infty = 0.729$, $\alpha = 2.31°$ and $Re_c = 6.5 \times 10^6$).
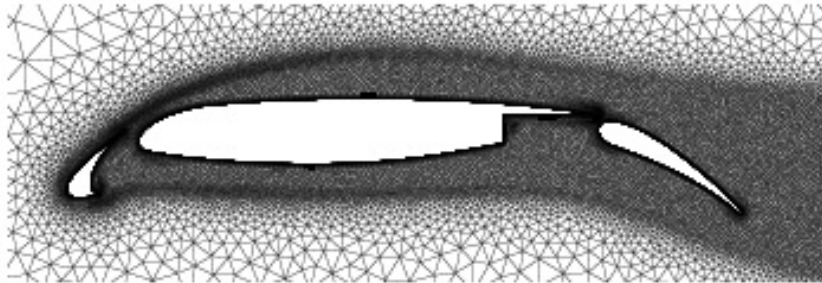

Figure 11: Medium grid for the MDA 30P-30N multi-element aerofoil

Convergence rates for higher order schemes with low-Mach number treatment don't exhibit particular improvement, however for second order not only the rate of convergence is faster but also the plateau is reached much lower. This trend is amplified for the residuals of the turbulence working variable as exemplified in figure 14, where the l^2 norms for the SA turbulence working variable ν and energy are plotted against the total number of iterations for the medium grid second order solutions.

Coefficients of drag and lift are plotted in figures 15 (a) and (b) respectively for all schemes against grid refinement. All solutions demonstrate monotone trends towards a grid independent solution for both drag
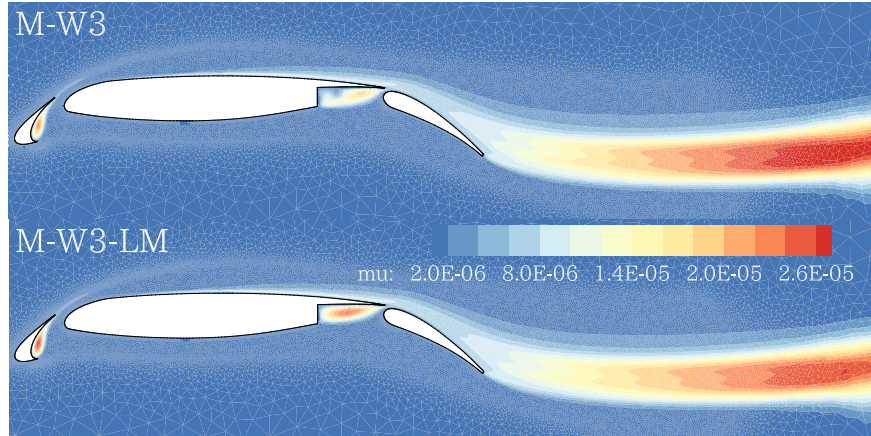
24

Figure 12: Contours of eddy viscosity (μ_t) for the medium grid W3 solutions, MDA 30P-30N aerofoil ($M_\infty = 0.2$, $\alpha = 16°$ and $Re_c = 9 \times 10^6$).

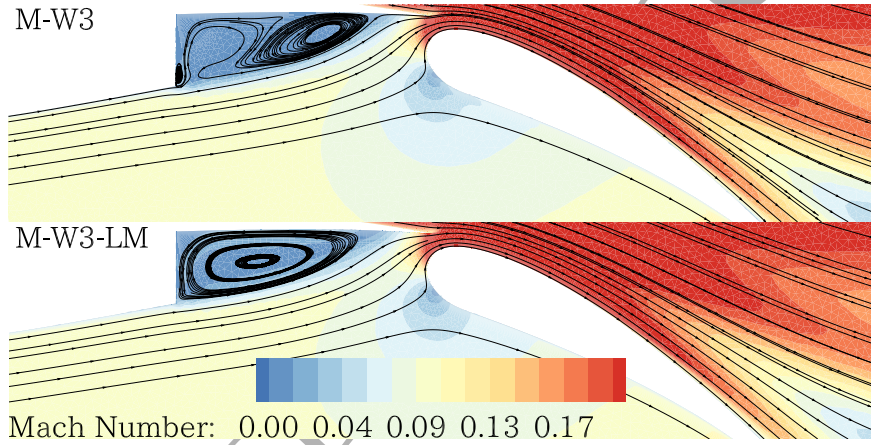
Figure 13: Contours of Mach number and streamlines for the medium grid W3 solutions, MDA 30P-30N aerofoil ($M_\infty = 0.2$, $\alpha = 16°$ and $Re_c = 9 \times 10^6$).

and lift except third and fifth order WENO without low-Mach number treatment on the fine grid. Higher resolution either by grid or polynomial order results to an increased lift and a decreased drag. The predicted Cl and Cd values agree well with values reported by other works [74] as well with the experimental lift coefficient of 4.1 (+/- 0.05) [70]. The advantage of the low-Mach number treatment is demonstrated for the two outliers mentioned earlier W3 and W5 on the fine grid, without the treatment the solution divergences and oscillations are observed in the wake which is due to the inherent unsteadiness of the solution at the flap wake, that the coupling of the turbulence model variable is not sufficient to produce the levels of eddy viscosity to supress these oscillations. This is again demonstrated when comparing the coefficient of pressure on the three elements with the M3 and W3 schemes against the experimental values in figure 16.
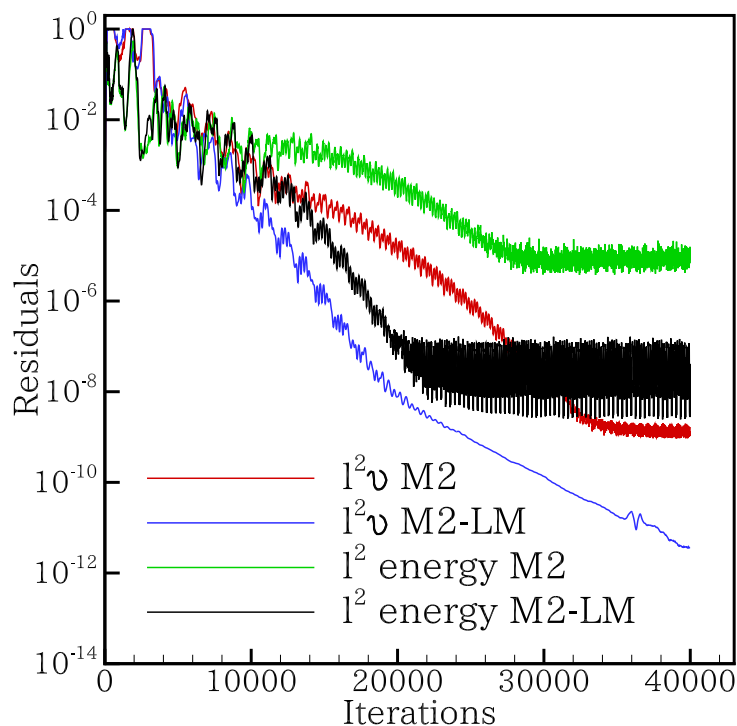
Figure 14: Residuals of turbulent variable ν and total energy for the second order solutions with and without low-Mach number treatment, MDA 30P-30N aerofoil ($M_\infty = 0.2$, $\alpha = 16°$ and $Re_c = 9 \times 10^6$).
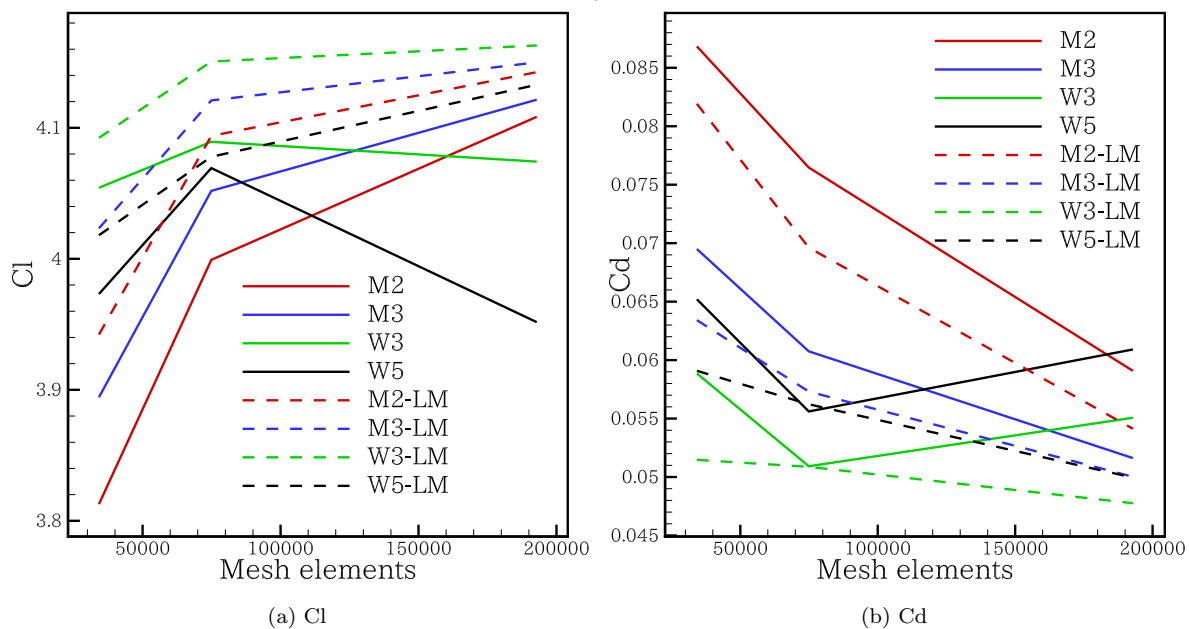

(a) Cl

(b) Cd

Figure 15: Lift and drag coefficients against grid points for the MDA 30P-30N aerofoil ($M_\infty = 0.2$, $\alpha = 16°$ and $Re_c = 9 \times 10^6$).
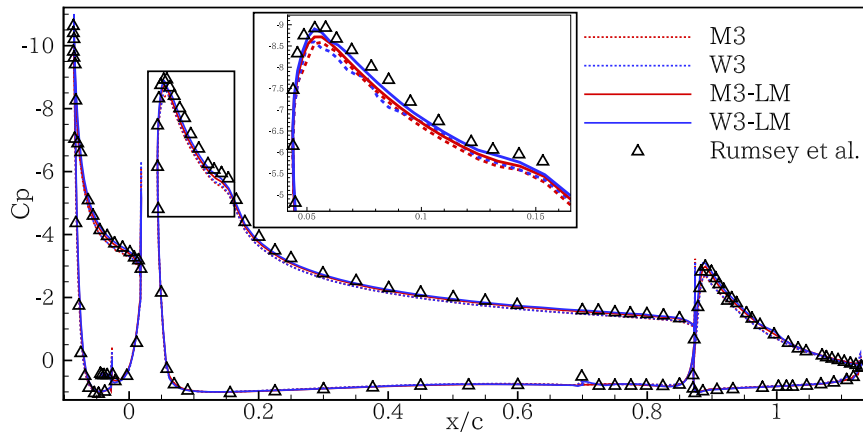
26

Figure 16: Coefficient of pressure for the coarse grid M3 and W3 solutions compared with experimental data [70], MDA 30P-30N aerofoil ($M_\infty = 0.2$, $\alpha = 16°$ and $Re_c = 9 \times 10^6$).

4.4. ONERA-M6

The three dimensional solver capabilities are assessed with the turbulent transonic flow around the ONERA-M6 wing; freestream conditions are set: Mach number of $M_\infty = 0.84$, an angle of attack of $a = 3.06°$ and a Reynolds number of $Re_c = 11.72 \times 10^6$ based on the mean aerodynamic chord. The ONERA-M6 is a swept-span wing, with no twist and symmetrical aerofoil section and a rounded tip. Wing tunnel measurements were conducted by Schmitt and Charpin [75] and pressure data are publicly available with an error margin for Cp of ± 0.02 . The transonic flow is characterised by a pair of λ-structured shocks on the upper surface of the wing where they coincide towards the wing tip.
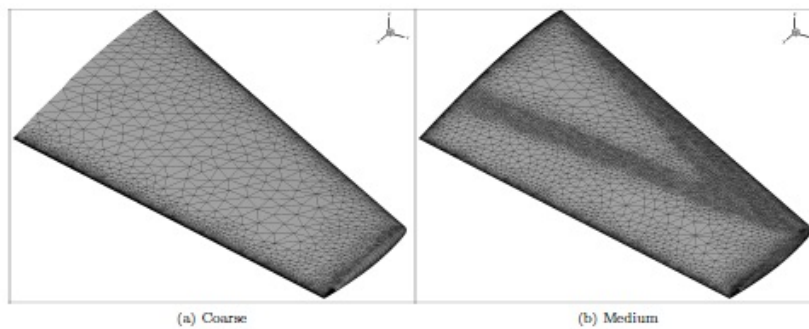

Figure 17: Grid topologies for the ONERA M6 wing.

Three grids are generated: coarse, medium and fine; triangular elements are used for the wing surface, projected normal to the wall to generate the prismatic layer followed by tetrahedra for the outer far field. Grid statistics are presented in table 4, the medium and fine grid are locally refined near the shock location as presented in figures 17.
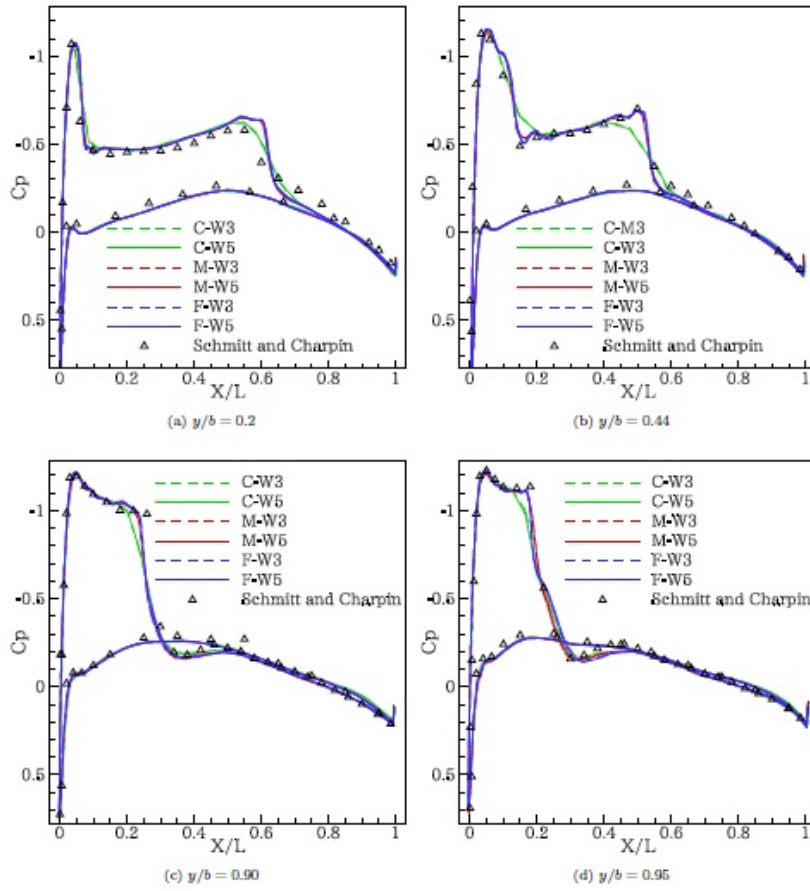
27

Figure 18: Coefficient of pressure for the W3 and W5 solutions at four spanwise stations compared with experimental data [75] ($M_\infty = 0.84$, $\alpha = 3.06°$ and $Re_c = 11.72 \times 10^6$).
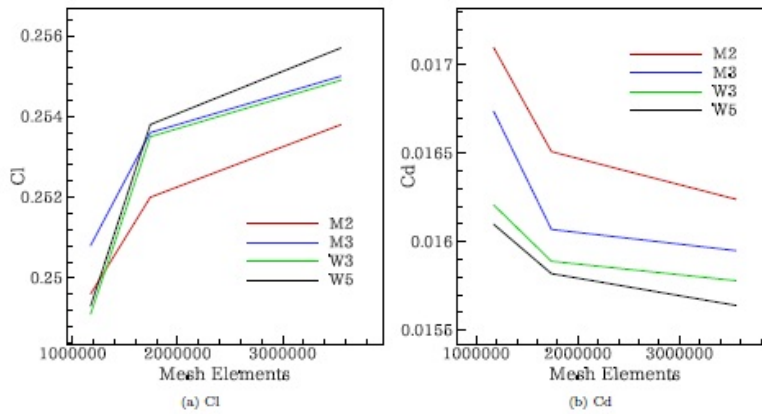

Figure 19: Lift and drag coefficients against grid points for the ONERA M6 wing ($M_\infty = 0.84$, $\alpha = 3.06°$ and $Re_c = 11.72 \times 10^6$).

28

Table 4: Grid properties for the ONERA M6 wing.

	Coarse	Medium	Fine
Elements	1,170,073	1,739,464	3,557,505
Triangles on wing's surface	38,389	43,720	69,692
y+	1.0	1.0	0.8

Grid resolution near the shock results in improved accuracy, sharper profiles and smaller discrepancies when compared with the experimental data [75], this can be depicted from the coefficient of pressure in figures 18, where the Cp is plotted at four spanwise sections where solutions of the WENO third and fifth order schemes are plotted for the three grid refinements. By either refining the grid or increasing the order of the scheme the predicted lift is increased and the drag decreased as shown in figure 18, where the Cl and Cd is plotted against grid size for all schemes. It is worth noting that higher order schemes (M3,W3 and W5) seem to converge within a narrower Cl and Cd range particularly for the finer grid resolutions, demonstrating that they reach grid-independent solutions faster than second order schemes.

4.5. CRM

This test case concerns the transonic flow over an aircraft configuration, the NASA Common Research Model (CRM) at cruise flight conditions. Drag prediction of the CRM model has been the main objective for the 4th, 5th and 6th drag prediction workshops [76, 77].
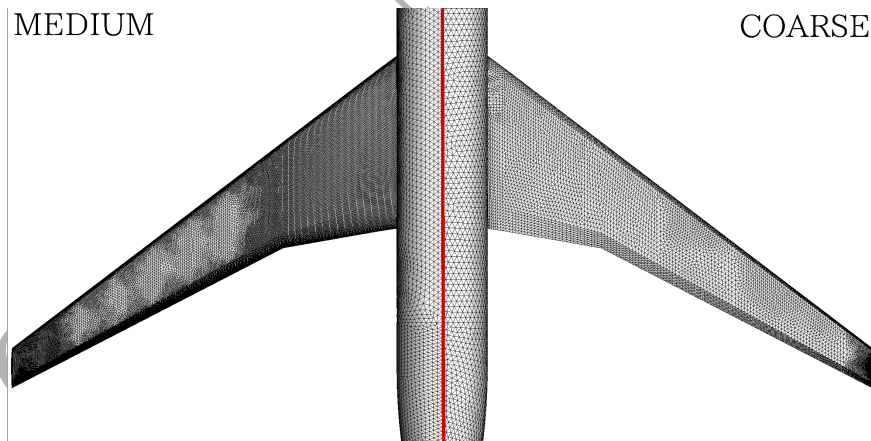

Figure 20: Grid configurations for the transonic flow over the CRM model.

Case 1a from the 4th workshop is considered for the current analysis, the CRM configuration includes wing, body and horizontal stabilizer. The flow is computed at a constant lift of $C_l = 0.5$ with error of ± 0.001. Wind tunnel measurement are carried out at the National Transonic Facility (NTF) at NASA Langley. The NTF data are publicly available which include drag polar, the corresponding coefficient of lift
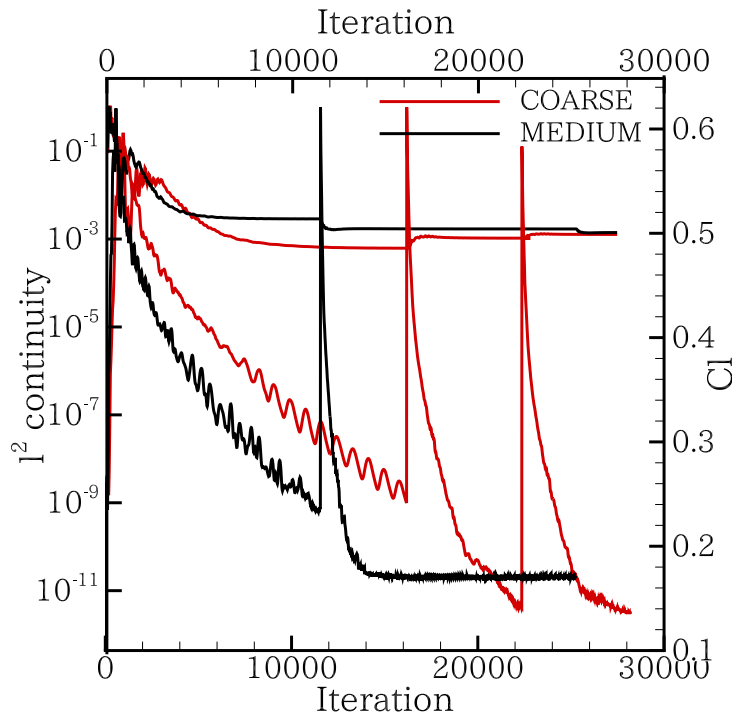
29

Figure 21: Continuity residuals and lift histories for the W3 solutions, CRM configuration ($M_\infty = 0.85$, $C_l = 0.5$ and $Re_c = 5.0 \times 10^6$).

and main wing pressure measurements at several spanwise stations. The freestream conditions correspond to a Mach number of $M = 0.85$ with a Reynolds number of 5×10^6 based on the reference chord length. Two grids are employed labelled as coarse and medium consisting of 3.5 and 11.0 million elements respectively, where the medium represents standard engineering practices; the grid surface distribution is shown in figure 20. The grid is locally refinement on the main wing and horizontal stabilizer.

The computations are initialised with an educated guess on the angle of attack, after the simulation has converged the angle is extrapolated for the first run and then linearly interpolated until the target lift is reached within the lift threshold. An example of the computations procedure is shown in figure 21 where the l^2 norm of continuity and the Cl histories are plotted. A residual drop of at least ten orders of magnitude is achieved for both grids for the W3 scheme. According to the findings of the two dimensional transonic flow case RAE-2822 presented in the previous sections, the results with the third order MUSCL reconstruction did not demonstrate noticeable benefits compared with the second order solutions, in terms of shock location and forces predictions. Therefore, for the present transonic case the main objective is to assess the WENO third and fifth order methods and compare them with the industry workhorse-second order upwind solution as well with reference experimental and CFD data.

30

The coefficient of pressure on the CRM configuration is shown in figure 22 and at two representative spanwise stations on the main wing in figure 23. The third and fifth order profiles are plotted against the chord-wise length and compared with the NTF pressure measurements [76]. The presence of the shock on the wing's suction side is evident for both stations near the wing's mid-spanwise location. Grid refinement suggests smaller discrepancies with respect to the shock position ($\eta = 0.60$) compared with the experiment regardless the scheme.

Table 5: Computed Drag for all schemes and grids compared with the average CFD and experimental values [76].

	Elements (10^6)	a	C_d	ΔC_d (counts)
C-M2	3.5	2.395	0.03227	47.6
C-W3	3.5	2.295	0.02962	21.11
C-W5	3.5	2.360	0.02942	19.06
M-M2	11.0	2.210	0.02810	5.89
M-W3	11.0	2.236	0.02742	0.93
M-W5	11.0	2.264	0.02716	3.49
DPW-CFD	-	2.340	0.02701	5
DPW-NTF	-	3.020	0.02751	-

Forces predictions are summarised in table 6, where for each run the angle of attack for constant lift, the predicted drag coefficient and the error ΔC_d in terms of drag counts with respect to the experiment [76] are presented. The first apparent observation for the predicted drag is that the standard deviation σ for the fine grid is at least three times smaller than for the one on the coarse grid. Moreover, second order drag estimates, irrespective of the grid, have at least twice greater σ compared with WENO predictions. Both WENO solutions on the fine grid suggest lower ΔC_d than 5 drag counts representing the averaged CFD predictions of the workshop data [76]. Considering the additional computational cost of the fifth order scheme and the associated gains in terms of accuracy for the subject test-case, the W3 scheme represents a more suitable method with a favourable balance between cost and accuracy for these type of configurations.

4.6. DLR-F11

Following the series of computations with the two dimensional high-lift device (MDA 30P-30N), the flow around the DLR-F11, a full aircraft configuration at landing conditions is computed. According to the findings from the CRM case, the W3 method was found to be the best compromise in terms of resources/cost, henceforth, the second and third order schemes would be employed for the DLR-F11 flow problem. In addition, the effect of the low-Mach number treatment technique is assessed. The increased complexity of the configuration lies with the flow conditions at high-angles of attack, the geometry itself as well as the grid size and quality, where high aspect ratio elements ($> 10,000$) with non-planar face definition
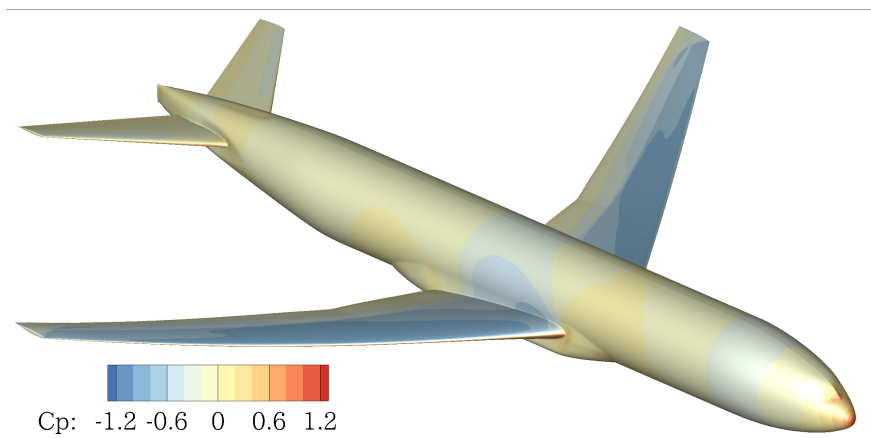
31

Figure 22: Coefficient of pressure on the medium grid W3 solutions, CRM configuration ($M_\infty = 0.85$, $C_l = 0.5$ and $Re_c = 5.0 \times 10^6$).
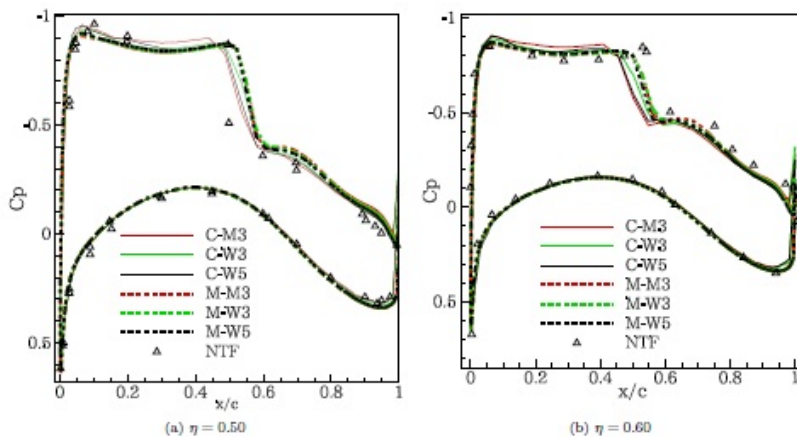

(a) $\eta = 0.50$

(b) $\eta = 0.60$

Figure 23: Coefficient of pressure at two spanwise stations (η) on the main wing compared with the wind tunnel measurement [76], CRM configuration ($M_\infty = 0.85$, $C_l = 0.5$ and $Re_c = 5.0 \times 10^6$).

are unavoidable. The grid sensitivity is more profound for high-order finite volume spatial methods as imbalanced sized stencils in the vicinity of sharp corners could lead to deteriorated accuracy even "blow-up" of the entire simulation process. Therefore, fifth-order solutions are not presented in the paper, converged solutions were only achieved by p-adaptation, decrease the polynomial order of the spatial reconstruction scheme near the wall surfaces. P-adaptivity is beyond this work focus as one of the current objectives is to assess the impact of the numerical schemes in terms of solution accuracy.

Case 1, configuration 2 of the 2nd AIAA high-lift prediction workshop [78] is considered with freestream conditions corresponding to a Mach number of $M_\infty = 0.175$, and angle of attack of $a = 16.0°$ and Reynolds number of $Re_c = 15.1 \times 10^6$ based on the mean aerodynamic chord. The computations were performed on a mixed-element unstructured grid containing approximately 27 million elements shown in figures 24. It
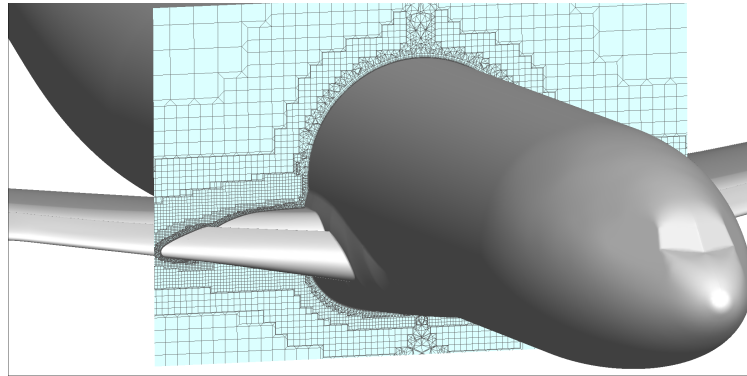
(a) Cut section of grid (mirrored).
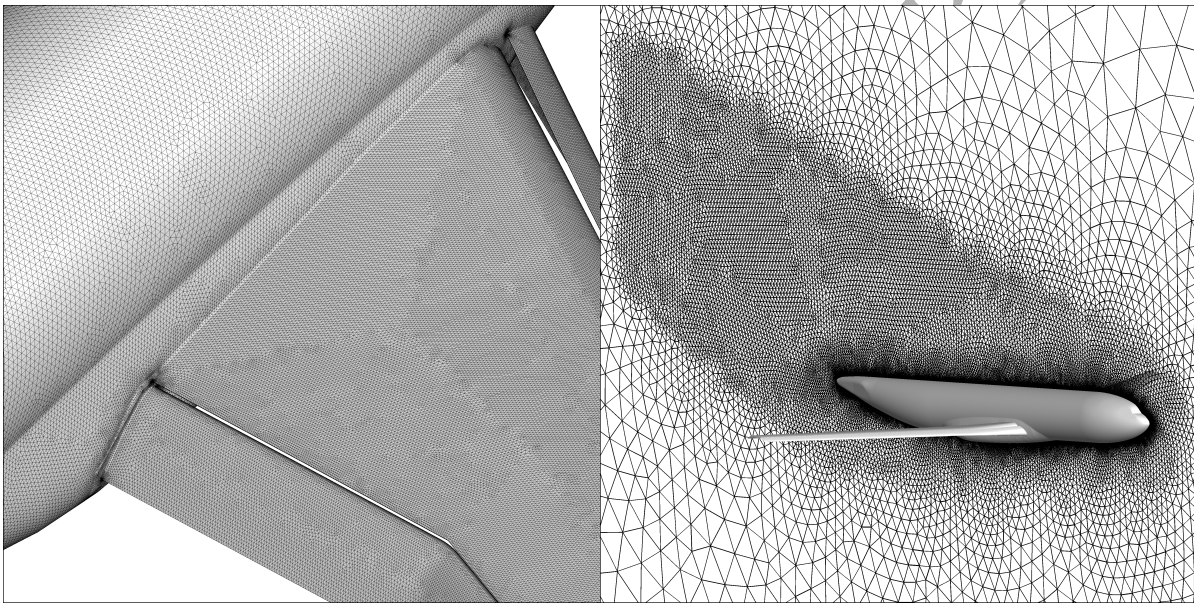
(b) Surface grid on the wing.

(c) Adapted grid in the wake.

Figure 24: Grid views for the DLR-F11 configuration.

should be mentioned that the simulated aircraft configuration is a simplified version of the full experimental configuration that included the slat-track and flap-track fairings and the slat pressure tubes. Simulations were carried out using the M2, M3 and W3 schemes. Additionally, low-Mach (LM) corrections were employed to study the reduction of numerical dissipation of the upwind schemes in the very low speed regions.

The employment of low-Mach number correction suggests improved lift predictions, thus also improving the lift to drag ratio see Table 6. The over-prediction of the drag coefficient compared to the experiment has been reported in several papers dealing with the same configuration at 16 degrees [79–81]. The discrepancies between drag predictions and computations have been partially attributed to installations effects of the model in the wind tunnel [82]. The scatter of the lift coefficient predictions using the M3 and W3 schemes in

33

Table 6: Coefficients of lift and drag compared with experimental data [78] and wall-clock time (hours) on 64 cores of Intel E5-2660 CPUs, DLR-F11 configuration.

	Time	C_L	C_D	C_L/C_D
Experiment	-	2.6796	0.2755	9.7278
M2	22.1	2.5514	0.3002	8.4984
M2-LM	22.1	2.6572	0.3043	8.7328
M3	26.5	2.5822	0.2993	8.6276
M3-LM	26.5	2.6842	0.3044	8.8171
W3	41.9	2.6197	0.3016	8.6857
W3-LM	41.9	2.6977	0.3047	8.8522

conjunction with the LM correction is 0.54%. This is an indication that the level of uncertainty is reduced when using higher than second order schemes. In terms of computational cost the M3 method is 20% and the W3 is 100% more expensive than the second order scheme.

The pressure coefficient at four indicative stations along the half-span wing is shown in figures 25; η is the percentage of the half-span length from the root to the wing tip. The suction peak near the wing root (η=28.8%) for the slat and main elements is under-predicted by all schemes; however, the WENO predictions are in better agreement with the experiment. This is also shown in the close-up plots. Furthermore, the LM-corrected WENO scheme gives better results near the wing tip (η=81.8% and η=89.1%) in the pressure recovery region of the slat and main-elements.

Although for turbulent flows at high angles of attack of massively separated flow RANS methods experience difficulties in providing the accurate solutions due to the inherent flow unsteadiness, and unsteady flow separation and turbulent wakes, in particular, they remain a high-fidelity engineering tool for assessing the impact of various design configurations. In this context the third order methods can increase the accuracy of these predictions and reduce the computational cost since coarser grid resolutions could be employed.

5. Conclusions

An investigation of the accuracy and efficiency of high-order k-exact finite volume, MUSCL and WENO schemes in conjunction with mixed element unstructured grids for RANS computations of aeronautical flows around simple and complex geometries, is presented. The evident outcome of the investigation lies with the overall potential increase of accuracy with higher-order discretisation. However, there is a limit on how much the RANS simulations can benefit from higher-order schemes, since the approximations in terms of turbulence models employed, implicit-time stepping algorithms, and elements of poor grid quality restricts the potential benefits of very high-order methods for these simulations. For the fifth-order scheme a greater sensitivity to grid irregularities and anisotropies is found; in addition, the imbalance between Jacobian
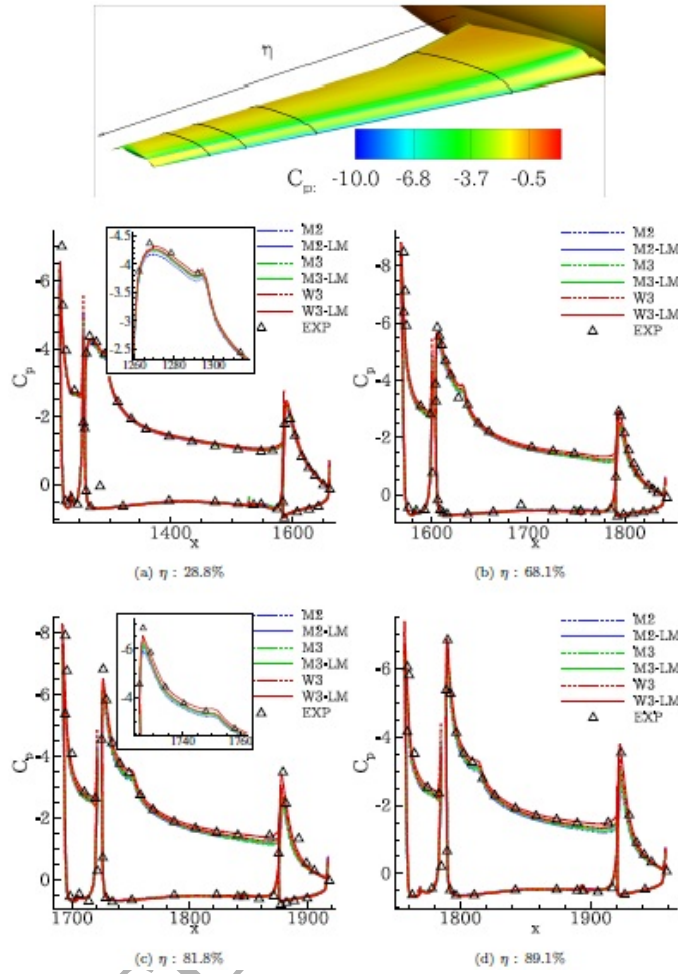
34

Figure 25: Pressure coefficient at four stations along the half-span model compared against the wind tunnel measurement data [78], DLR-F11 configuration ($M_\infty = 0.175$, $\alpha = 16°$ and $Re = 15.1 \times 10^6$).

approximations of the implicit time stepping and the spatial-discretisation, and the excessive computational cost do not justify their applicability for practical industrial-scale RANS simulations. The WENO third-order method provides the best trade/off in terms of accuracy cost and robustness for most cases. Coupling the discretisation of turbulence model with the mean flow equations for the WENO reconstruction suggests improved convergence and accuracy compared with standard practices of lower order methods. Furthermore, the proposed Low-Mach number treatment technique for compressible solvers, provides enhanced accuracy irrespective of spatial scheme type or order without additional computational effort. Two-equation models such as the k-ω SST [83] are currently under implementation and will be assessed and compared with the results of this work. Furthermore, the benefits of using higher-order schemes for RANS simulations, could

35

also be useful when dealing with Detached Eddy Simulations (DES) and the discretisation for both RANS and LES regions being high-order, an aspect that is going to be explored in the near future.

Acknowledgements

References

[1] I. Kokkinakis, D. Drikakis, Implicit large eddy simulation of weakly-compressible turbulent channel flow, Computer Methods in Applied Mechanics and Engineering 287 (2015) 229–261. doi:10.1016/j.cma.2015.01.016.

[2] D. Drikakis, M. Hahn, A. Mosedale, B. Thornber, Large eddy simulation using high-resolution and high-order methods, Philosophical Transactions of the Royal Society A: Mathematical, Physical and Engineering Sciences 367 (1899) (2009) 2985–2997.

[3] P. Tsoutsanis, A. Antoniadis, D. Drikakis, WENO schemes on arbitrary unstructured meshes for laminar, transitional and turbulent flows, Journal of Computational Physics 256 (2014) 254–276.

[4] H. Huynh, Z. Wang, P. Vincent, High-order methods for computational fluid dynamics: A brief review of compact differential formulations on unstructured grids, Computers and Fluids 98 (2014) 209–220. doi:10.1016/j.compfluid.2013.12.007.

[5] Z. Wang, K. Fidkowski, R. Abgrall, F. Bassi, D. Caraeni, A. Cary, H. Deconinck, R. Hartmann, K. Hillewaert, H. Huynh, N. Kroll, G. May, P.-O. Persson, B. van Leer, M. Visbal, High-order CFD methods: Current status and perspective, International Journal for Numerical Methods in Fluids 72 (8) (2013) 811–845. doi:10.1002/fld.3767.

[6] F. Hindenlang, G. Gassner, C. Altmann, A. Beck, M. Staudenmaier, C. Munz, Explicit discontinuous Galerkin methods for unsteady problems, Computers and Fluids 61 (2012) 86–93.

[7] G. Gassner, F. Lorcher, C. Munz, A discontinuous Galerkin scheme based on a space-time expansion II. Viscous flow equations in multi dimensions, Journal of Scientific Computing 34 (3) (2008) 260–286.

[8] M. Dumbser, Arbitrary high order PNPM schemes on unstructured meshes for the compressible Navier-Stokes equations, Computers and Fluids 39 (1) (2010) 60–76. doi:10.1016/j.compfluid.2009.07.003.

[9] M. Dumbser, D. Balsara, E. Toro, C.-D. Munz, A unified framework for the construction of one-step finite volume and discontinuous Galerkin schemes on unstructured meshes, Journal of Computational Physics 227 (18) (2008) 8209–8253. doi:10.1016/j.jcp.2008.05.025.

[10] H. Luo, L. Luo, R. Nourgaliev, V. Mousseau, N. Dinh, A reconstructed discontinuous Galerkin method for the compressible Navier-Stokes equations on arbitrary grids, Journal of Computational Physics 229 (19) (2010) 6961–6978. doi:10.1016/j.jcp.2010.05.033.

[11] N. Burgess, D. Mavriplis, Hp-adaptive discontinuous Galerkin methods for the Navier-Stokes equations, AIAA Journal 50 (12) (2012) 2682–2694.

[12] M. Ceze, K. Fidkowski, A robust adaptive solution strategy for high-order implicit CFD solvers, in: 20th AIAA Computational Fluid Dynamics Conference, 2011.

[13] A. Harten, B. Engquist, S. Osher, S. R. Chakravarthy, Uniformly high order accurate Essentially Non-Oscillatory schemes, III, Journal of Computational Physics 71 (2) (1987) 231–303.

[14] C. Shu, S. Osher, Efficient implementation of essentially non-oscillatory shock-capturing schemes, Journal of Computational Physics 77 (2) (1988) 439–471.

[15] G. Jiang, C. W. Shu, Efficient implementation of weighted ENO schemes, Journal of Computational Physics 126 (1) (1996) 202–228.

[16] J. Huang, H. Lin, J. Yang, Implicit preconditioned WENO scheme for steady viscous flow computation, Journal of Computational Physics 228 (2) (2009) 420–438.

[17] J. Yang, T. Hsieh, C. Wang, Implicit weighted essentially nonoscillatory schemes with antidiffusive flux for compressible viscous flows, AIAA Journal 47 (6) (2009) 1435–1444.

[18] O. Friedrich, Weighted Essentially Non-Oscillatory schemes for the interpolation of mean values on unstructured grids, Journal of Computational Physics 144 (1) (1998) 194–212.

[19] W. Wolf, J. Azevedo, High-order unstructured essentially nonoscillatory and weighted essentially nonoscillatory schemes for aerodynamic flows, AIAA Journal 44 (10) (2006) 2295–2310.

[20] M. Dumbser, W. Boscheri, High-order unstructured Lagrangian one-step WENO finite volume schemes for non-conservative hyperbolic systems: Applications to compressible multi-phase flows, Computers and Fluids 86 (2013) 405–432.

[21] C. Ollivier-Gooch, M. Van Altena, A high-order-accurate unstructured mesh Finite-Volume scheme for the advection-diffusion equation, Journal of Computational Physics 181 (2) (2002) 729–752.

[22] D. Caraeni, D. C. Hill, Unstructured-grid third-order finite volume discretization using a multistep quadratic data-reconstruction method, AIAA Journal 48 (4) (2010) 808–817.

[23] P. Tsoutsanis, V. A. Titarev, D. Drikakis, WENO schemes on arbitrary mixed-element unstructured meshes in three space dimensions, Journal of Computational Physics 230 (4) (2011) 1585–1601.

[24] A. Antoniadis, P. Tsoutsanis, Drikakis.D., High-order schemes on mixed-element unstructured grids for aerodynamic flows, in: AIAA (Ed.), 42nd AIAA Fluid Dynamics Conference and Exhibit, no. AIAA 2012-2833, New Orleans, Louisiana, 2012.

[25] A. F. Antoniadis, P. Tsoutsanis, D. Drikakis, Numerical Accuracy in RANS Computations of High-Lift Multi-element Airfoil and Aircraft Configurations, in: AIAA (Ed.), 53rd AIAA Aerospace Sciences Meeting, no. AIAA 2015-0317, Kissimmee, Florida, 2015.

[26] D. Drikakis, A. F. Antoniadis, P. Tsoutsanis, I. Kokkinakis, Z. Rana, Azure: An advanced cfd software suite based on high-resolution and high-order methods, in: AIAA (Ed.), 53rd AIAA Aerospace Sciences Meeting, no. AIAA 2015-0813, Kissimmee, Florida, 2015.

[27] D. Balsara, C. Altmann, C. Munz, M. Dumbser, A sub-cell based indicator for troubled zones in RKDG schemes and a novel class of hybrid RKDG+HWENO schemes, Journal of Computational Physics 226 (1) (2007) 586–620.

[28] J. Zhu, J. Qiu, C. Shu, M. Dumbser, Runge-Kutta discontinuous Galerkin method using WENO limiters II: Unstructured meshes, Journal of Computational Physics 227 (9) (2008) 4330–4353.

[29] V. Titarev, E. Toro, ADER schemes for three-dimensional non-linear hyperbolic systems, Journal of Computational Physics 204 (2) (2005) 715–736. doi:10.1016/j.jcp.2004.10.028.

[30] H. Luo, J. Baum, R. Lohner, A Hermite WENO-based limiter for discontinuous Galerkin method on unstructured grids, Journal of Computational Physics 225 (1) (2007) 686–713. doi:10.1016/j.jcp.2006.12.017.

[31] A. Uranga, P. Persson, M. Drela, J. Peraire, Implicit Large Eddy Simulation of transition to turbulence at low Reynolds numbers using a Discontinuous Galerkin method, International Journal for Numerical Methods in Engineering 87 (1-5) (2011) 232–261.

[32] B. Thornber, A. Mosedale, D. Drikakis, D. Youngs, R. Williams, An improved reconstruction method for compressible flows with low Mach number features, Journal of Computational Physics 227 (10) (2008) 4873–4894.

[33] P. Tsoutsanis, I. Kokkinakis, L. Konozsy, D. Drikakis, R. Williams, D. Youngs, An investigation of the accuracy and efficiency of structured and unstructured, compressible and incompressible methods for the vortex pairing problem, Computer Methods in Applied Mechanics and Engineering 293 (2015) 207–231.

[34] J. Housman, C. Kiris, M. Hafez, Preconditioned methods for simulations of low speed compressible flows, Computers and Fluids 38 (7) (2009) 1411–1423. doi:10.1016/j.compfluid.2008.01.034.

[35] E. Turkel, R. Radespiel, N. Kroll, Assessment of preconditioning methods for multidimensional aerodynamics, Computers and Fluids 26 (6) (1997) 613–634.

[36] C. Kiris, J. Housman, D. Kwak, Space/time convergence analysis of a ignition overpressure in the flame trench, in: CFD Review 2010, World Scientific, 2010.

[37] A. Garcia-Uceda Juarez, A. Raimo, E. Shapiro, B. Thornber, Steady turbulent flow computations using a low mach fully compressible scheme, AIAA Journal 52 (11) (2014) 2559–2575. doi:10.2514/1.J052948.

[38] N. K. Burgess, D. J. Mavriplis, Robust computation of turbulent flows using a Discontinuous Galerkin Method, in: AIAA (Ed.), 50th Aerospace Sciences Meeting and Exhibit, no. AIAA 2012-0457, 2012.

[39] T. Oliver, D. Darmofal, Impact of turbulence model irregularity on high-order discretizations, in: AIAA (Ed.), 47th AIAA Aerospace Sciences Meeting Including The New Horizons Forum and Aerospace Exposition, no. AIAA 2009-953, Orlando, Florida, 2009.

[40] S. Yoon, D. Kwak, Three-dimensional incompressible Navier-Stokes solver using lower-upper symmetric-Gauss-Seidel algorithm, AIAA journal 29 (6) (1991) 874–875.

[41] H. Luo, J. Baum, R. Lohner, A fast, matrix-free implicit method for compressible flows on unstructured grids, Journal of Computational Physics 146 (2) (1998) 664–690.

[42] P. R. Spalart, S. R. Allmaras, One-equation turbulence model for aerodynamic flows, Recherche Aerospatiale (1) (1994) 5–21.

[43] T. Barth, P. Frederickson, Higher order solution of the Euler equations on unstructured grids using quadratic reconstruction, AAIA, Aerospace sciences meeting January 1990 12 (90-0013).

[44] M. Dumbser, M. Kaser, Arbitrary high order Non-Oscillatory Finite Volume schemes on unstructured meshes for linear hyperbolic systems, Journal of Computational Physics 221 (2) (2007) 693–723.

[45] T. Barth, D. Jespersen, The design and application of upwind schemes on unstructured meshes, AAIA, Aerospace Science Meeting 89 (0366).

[46] E. F. Toro, Riemann Solvers and Numerical Methods for Fluid Dynamics, 3rd Edition, Springer, 2009.

[47] L. Ivan, C. Groth, High-order solution-adaptive central essentially non-oscillatory (CENO) method for viscous flows, Journal of Computational Physics 257 (PA) (2014) 830–862. doi:10.1016/j.jcp.2013.09.045.

[48] G. Gassner, F. Lorcher, C. Munz, A contribution to the construction of diffusion fluxes for finite volume and discontinuous Galerkin schemes, Journal of Computational Physics 224 (2) (2007) 1049–1063.

[49] H. Liu, J. Yan, The direct discontinuous Galerkin (DDG) methods for diffusion problems, SIAM Journal on Numerical

Analysis 47 (1) (2008) 675–698.

[50] H. Liu, J. Yan, The direct discontinuous Galerkin (DDG) method for diffusion with interface corrections, Communications in Computational Physics 8 (3) (2010) 541–564.

[51] V. Titarev, D. Drikakis, Uniformly high-order schemes on arbitrary unstructured meshes for advection-diffusion equations, Computers and Fluids 46 (1) (2011) 467–471.

[52] I. Cueto-Felgueroso, L.and Colominas, X. Nogueira, F. Navarrina, M. Casteleiro, Finite volume solvers and Moving Least-Squares approximations for the compressible Navier-Stokes equations on unstructured grids, Computer Methods in Applied Mechanics and Engineering 196 (45-48) (2007) 4712–4736.

[53] B. Diskin, J. L. Thomas, E. J. Nielsen, H. Nishikawa, J. A. White, Comparison of node-centered and cell-centered unstructured finite-volume discretizations: Viscous fluxes, AIAA Journal 48 (7) (2010) 1326–1338.

[54] A. F. Antoniadis, D. Drikakis, I. Kokkinakis, P. Tsoutsanis, Z. Rana, High-order methods for hypersonic shock wave turbulent boundary layer interaction flow, in: AIAA (Ed.), 20th AIAA International Space Planes and Hypersonic Systems and Technologies Conference, no. AIAA 2015-3524, Glasgow, Scotland, 2015.

[55] A. Jameson, S. Yoon, Lower-upper implicit schemes with multiple grids for the Euler equations, AIAA journal 25 (7) (1987) 929–935.

[56] M. Parsani, K. Van den Abeele, C. Lacor, E. Turkel, Implicit lu-sgs algorithm for high-order methods on unstructured grid with p-multigrid strategy for solving the steady navier-stokes equations, Journal of Computational Physics 229 (3) (2010) 828–850.

[57] K. Nakahashi, D. Sharov, S. Kano, M. Kodera, Applications of unstructured hybrid grid method to high-reynolds number viscous flows, International Journal for Numerical Methods in Fluids 31 (1) (1999) 97–111.

[58] T. Haga, K. Sawada, Z. J. Wang, An implicit LU-SGS scheme for the spectral volume method on unstructured tetrahedral grids, Communications in Computational Physics 6 (5) (2009) 978–986.

[59] G. Hu, R. Li, T. Tang, A robust WENO type finite volume solver for steady Euler equations on unstructured grids, Communications in Computational Physics 9 (3) (2011) 627–648.

[60] R. Chen, Z. Wang, Fast, block lower-upper symmetric Gauss-Seidel scheme for arbitrary grids, AIAA journal 38 (12) (2000) 2238–2245.

[61] Y. Sun, Z. Wang, Y. Liu, Efficient implicit non-linear LU-SGS approach for compressible flow computation using high-order spectral difference method, Communications in Computational Physics 5 (2-4) (2009) 760–778.

[62] P. Persson, J. Peraire, Newton-GMRES preconditioning for discontinuous Galerkin discretizations of the Navier-stokes equations, SIAM Journal on Scientific Computing 30 (6) (2008) 2709–2733.

[63] P. Batten, M. Leschziner, U. Goldberg, Average-state Jacobians and implicit methods for compressible viscous and turbulent flows, Journal of Computational Physics 137 (1) (1997) 38–78.

[64] J. Thiber, M. Crandjacques, L. Ohman, Experimental data base for computer program assessment, Tech. Rep. AGARD-AR-138/A1 (1979).

[65] P. Cook, M. McDonald, M. Firmin, Experimental data base for computer program assessment, Tech. Rep. AGARD-AR-138/A6 (1979).

[66] D. Mavriplis, L. Matinelli, Multigrid solution of compressible turbulent flow on unstructured meshes using a two-equation model, International Journal for Numerical Methods in Fluids 18 (10) (1994) 887–914.

[67] S. R. Allmaras, J. F.T., S. P. R., Modifications and clarifications for the implementation of the Spalart-Allmaras turbulence model, in: 7th International Conference on Computational Fluid Dynamics (ICCFD7), no. ICCFD7-1902, Big Island, Hawaii, USA, 2012.

[68] J. ZhenHua, Y. Chao, Y. Jian, Q. Feng, Y. Wu, A Spalart-allmaras Turbulence Model Implementation for High-order Discontinuous Galerkin Solution of the Reynolds-averaged Navier-stokes Equations, Flow, Turbulence and Combustion 96 (3) (2016) 623–638. doi:10.1007/s10494-015-9656-7.

[69] F. W. Spaid, High reynolds number, multielement airfoil flowfield measurements, Journal of Aircraft 37 (3) (2000) 499–507.

[70] C. L. Rumsey, E. M. Lee Rausch, R. D. Watson, Three-dimensional effects in multi-element high lift computations, Computers and Fluids 32 (5) (2003) 631–657.

[71] S. E. Rogers, F. Menter, P. A. Durbin, N. N. Mansour, A comparison of turbulence models in computing multi-element airfoil flows, AIAA Journal (94-0291).

[72] W. K. Anderson, D. L. Bonhaus, R. J. McGhee, B. S. Walker, Navier-Stokes computations and experimental comparisons for multielement airfoil configurations, Journal of Aircraft 32 (6) (1995) 1246–1253.

[73] S. Kim, J. J. Alonso, A. Jameson, Multi-element high-lift configuration design optimization using viscous continuous adjoint method, Journal of Aircraft 41 (5) (2004) 1082–1097.

[74] N. Burgess, D. Mavriplis, High-order Discontinuous Galerkin methods for turbulent high-lift flows, in: Seventh International Conference on Computational Fluid Dynamics, no. ICCFD7-4202, 2012.

[75] V. Schmitt, F. Charpin, Pressure Distributions on the ONERA-M6-Wing at Transonic Mach Numbers, Tech. Rep. AGARD-AR-138 (1979).

[76] J. Vassberg, E. Tinoco, M. Mani, B. Rider, T. Zickuhr, D. Levy, O. Brodersen, B. Eisfeld, S. Crippa, R. Wahls, J. Morrison, D. Mavriplis, M. Murayama, Summary of the fourth AIAA computational fluid dynamics drag prediction workshop, Journal of Aircraft 51 (4) (2014) 1070–1089. doi:10.2514/1.C032418.

[77] D. Levy, K. Laflin, E. Tinoco, J. Vassberg, M. Mani, B. Rider, C. Rumsey, R. Wahls, J. Morrison, O. Brodersen, S. Crippa, D. Mavriplis, M. Murayama, Summary of data from the fifth AIAA CFD drag prediction workshop, 2013.

[78] C. Rumsey, J. Slotnicky, Overview and summary of the second AIAA High Lift Prediction Workshop, in: 52nd AIAA Aerospace Sciences Meeting - AIAA Science and Technology Forum and Exposition, SciTech 2014, 2014.

[79] P. Eliasson, S. H. Peng, Results from the 2nd AIAA CFD high lift prediction workshop using EDGE, in: 52nd AIAA

Aerospace Sciences Meeting - AIAA Science and Technology Forum and Exposition, SciTech 2014, 2014.

[80] E. Lee-Rausch, C. Rumsey, M. Park, Grid-adapted FUN3D computations for the second high lift prediction workshop , in: 32nd AIAA Applied Aerodynamics Conference, 2014.

[81] R. Rudnik, S. Melber-Wilkending, DLR Contribution to the 2nd High Lift Prediction Workshop, in: 52nd AIAA Aerospace Sciences Meeting - AIAA Science and Technology Forum and Exposition, SciTech 2014, 2014.

[82] P. Eliasson, Investigation of a half-model high-lift configuration in a wind tunnel, Journal of Aircraft 45 (1) (2008) 29–37.

[83] F. Menter, Two-equation eddy-viscosity turbulence models for engineering applications, AIAA journal 32 (8) (1994) 1598–1605.